

DTIC FILE COPY

06-8602/5

(4)

N00014-85-C-0206  
NR 039-283 DATED 12/21/84

AD-A203 593

# MICROMECHANISMS OF FATIGUE CRACK GROWTH AND FRACTURE TOUGHNESS IN METAL MATRIX COMPOSITES

Technical Report for the Period 08/01/88 to 12/31/88

Prepared For

Office of Naval Research  
800 North Quincy St.  
Arlington, VA 22217

By D. L. Davidson

Southwest Research Institute  
P. O. Box 28510  
San Antonio, TX 78284

DTIC  
ELECTE  
JAN 20 1989  
S  
D

January 1989

Reproduction in whole or in part is permitted for any purpose of the United States Government

DISTRIBUTION STATEMENT A  
Approved for public release;  
Distribution Unlimited



SOUTHWEST RESEARCH INSTITUTE  
SAN ANTONIO  
HOUSTON

80 1 25 088

N00014-85-C-0206  
NR 039-283 DATED 12/21/84

# MICROMECHANISMS OF FATIGUE CRACK GROWTH AND FRACTURE TOUGHNESS IN METAL MATRIX COMPOSITES

Technical Report for the Period 08/01/88 to 12/31/88

Prepared For

Office of Naval Research  
800 North Quincy St.  
Arlington, VA 22217

By D. L. Davidson

Southwest Research Institute  
P. O. Box 28510  
San Antonio, TX 78284

January 1989

Reproduction in whole or in part is permitted for any purpose of the United States Government



Accession For	
THIS CRACK	<input checked="" type="checkbox"/>
DTIC TAB	<input type="checkbox"/>
Unannounced	<input type="checkbox"/>
Justification	
By	
Date	
Availability Codes	
Dist	Avail and/or
A-1	

SECURITY CLASSIFICATION OF THIS PAGE

## REPORT DOCUMENTATION PAGE

1a. REPORT SECURITY CLASSIFICATION <b>Unclassified</b>			1b. RESTRICTIVE MARKINGS									
2a. SECURITY CLASSIFICATION AUTHORITY			3. DISTRIBUTION / AVAILABILITY OF REPORT  <b>Unlimited</b>									
2b. DECLASSIFICATION / DOWNGRADING SCHEDULE												
4. PERFORMING ORGANIZATION REPORT NUMBER(S) <b>06-8602/5</b>			5. MONITORING ORGANIZATION REPORT NUMBER(S) <b>-4313283-02</b>									
6a. NAME OF PERFORMING ORGANIZATION <b>Southwest Research Institute</b>		6b. OFFICE SYMBOL (If applicable)	7a. NAME OF MONITORING ORGANIZATION <b>Dr. Steven G. Fishman - Code 431N Office of Naval Research</b>									
6c. ADDRESS (City, State, and ZIP Code) <b>6220 Culebra Road San Antonio, TX 78284</b>		7b. ADDRESS (City, State, and ZIP Code) <b>800 North Quincy Street Arlington, VA 22217-5000</b>										
8a. NAME OF FUNDING / SPONSORING ORGANIZATION <b>Office of Naval Research</b>		8b. OFFICE SYMBOL (If applicable)	9. PROCUREMENT INSTRUMENT IDENTIFICATION NUMBER <b>N00014-85-C-0206</b>									
8c. ADDRESS (City, State, and ZIP Code) <b>800 North Quincy Street Arlington, VA 22217-5000</b>		10. SOURCE OF FUNDING NUMBERS <table border="1"><tr><td>PROGRAM ELEMENT NO.</td><td>PROJECT NO.</td><td>TASK NO.</td><td>WORK UNIT ACCESSION NO.</td></tr><tr><td></td><td></td><td></td><td></td></tr></table>			PROGRAM ELEMENT NO.	PROJECT NO.	TASK NO.	WORK UNIT ACCESSION NO.				
PROGRAM ELEMENT NO.	PROJECT NO.	TASK NO.	WORK UNIT ACCESSION NO.									
11. TITLE (Include Security Classification) <b>Micromechanisms of Crack Growth and Fracture Toughness in Metal Matrix Composites</b>												
12. PERSONAL AUTHOR(S) <b>D.L. Davidson</b>												
13a. TYPE OF REPORT <b>Technical</b>		13b. TIME COVERED <b>FROM 08/01/88 to 12/31/88</b>	14. DATE OF REPORT (Year, Month, Day) <b>January 1989</b>	15. PAGE COUNT <b>58</b>								
16. SUPPLEMENTARY NOTATION												
17. COSATI CODES <table border="1"><tr><td>FIELD</td><td>GROUP</td><td>SUB-GROUP</td></tr><tr><td></td><td></td><td></td></tr></table>			FIELD	GROUP	SUB-GROUP				18. SUBJECT TERMS (Continue on reverse if necessary and identify by block number) <b>KEY WORDS: Metal matrix composites, silicon carbide reinforcement, fatigue crack growth, fracture toughness, particulate strengthening, crack growth micromechanisms. (JCS)</b>			
FIELD	GROUP	SUB-GROUP										
19. ABSTRACT (Continue on reverse if necessary and identify by block number) <p>A detailed micromechanics analysis has been performed on a composite of 2014 aluminum alloy matrix with 15 vol.% particulate SiC. This composite was manufactured by the Dural Co. by casting and extrusion. The matrix alloy was peak aged before testing. The microstructure was found to contain about 3% intermetallic particles in addition to those expected for this material. Fatigue cracks were grown from approximately threshold to rapid fracture stress intensities. Fatigue crack growth rates and fracture toughness were measured. Analyses of the crack tips were performed by stereoimaging at low and intermediate stress intensities, and just prior to the onset of rapid fracture. Detailed strain maps were derived, and considerable influence of SiC on strain was found. Analyses of microcracks near the main crack were made and found to have only a small influence on fracture. Fatigue threshold was explained on the basis of measured and calculated crack closure, but fracture toughness values measured could not be rationalized by fractography or by applying previously developed quantitative models.</p>												
20. DISTRIBUTION / AVAILABILITY OF ABSTRACT <input type="checkbox"/> UNCLASSIFIED/UNLIMITED <input checked="" type="checkbox"/> SAME AS RPT. <input type="checkbox"/> DTIC USERS			21. ABSTRACT SECURITY CLASSIFICATION <b>Unclassified</b>									
22a. NAME OF RESPONSIBLE INDIVIDUAL <b>David L. Davidson</b>			22b. TELEPHONE (Include Area Code) <b>512-522-2314</b>	22c. OFFICE SYMBOL								

## TABLE OF CONTENTS

	<u>Page</u>
List of Tables.....	iii
List of Figures.....	iv
Abstract.....	1
I. Introduction.....	1
II. Material.....	2
III. Tensile and Fracture Properties.....	4
Fractography.....	6
IV. Micromechanics.....	7
Fatigue at Low $\Delta K$ .....	7
Fatigue at Intermediate $\Delta K$ .....	9
Approach to $K_{IC}$ .....	11
V. Strain Distributions and Plastic Zone Sizes.....	11
VI. Discussion.....	13
Fatigue.....	14
Fracture Toughness.....	16
VII. Summary and Conclusions.....	18
Acknowledgments.....	19
References.....	19
Tables.....	21
Figures.....	26

## LIST OF TABLES

<u>Table</u>		<u>Page</u>
1	2014-PA+15v/o SiC Mechanical and Fracture Properties	22
2	Microcrack Analysis	23
3	Crack Driving Force Analysis	24
4	Strain Distributions and Plastic Zone Size	25

## LIST OF FIGURES

<u>Figure</u>	<u>Page</u>
1      Microstructure of 2014+15v/o SiC	27
2      Transmission electron microscopy of 2014-Pa+15v/o SiC	28
3      Measured distribution of SiC and intermetallic particles in 2014-PA+15v/o SiC	29
4a-b   (a) Stress-strain characteristics of two composite tensile specimens; (b) Stress-plastic strain curves for two specimens of the composite derived from Fig. 4(a)	30
5      Fatigue crack growth behavior of the composite	32
6      Crack growth sequence for a fatigue crack integrating with SiC particles	33
7a-b   (a) Crack length as a function of loading cycles for the crack path shown in Fig. 6; (b) Fatigue crack growth rates derived from the data in Fig. 7(a)	34
8      Fatigue crack growth path at intermediate $\Delta K = 16.2 \text{ MPa}\sqrt{\text{m}}$	36
9      Crack tips at about $\Delta K = 19 \text{ MPa}\sqrt{\text{m}}$ showing multiple non- connected microcracks	37
10     Crack tip on the cycle preceding fast fracture	38
11     Fractography of fatigue and fast fracture	39
12     Contour lines of maximum shear strain around the fatigue crack tip shown in Fig. 6(b), grown at $\Delta K = 8.8 \text{ MPa}\sqrt{\text{m}}$ , which is relatively remote to SiC particles (shown as hatched regions)	40
13a-b   (a) Contour lines of maximum shear strain round the fatigue crack shown in Fig. 6(c), grown at $\Delta K = 8.8 \text{ MPa}\sqrt{\text{m}}$ ; (b) A detail of the strains for the field in Fig. 13(a)	41
14     Distribution of maximum shear strain for the fatigue crack shown in Fig. 6(d), grown at $\Delta K = 8.8 \text{ MPa}\sqrt{\text{m}}$	43

## LIST OF FIGURES (continued)

15	Stresses computed from the strains shown in Fig. 14 showing the strong stress gradient across the matrix-particle interface	44
16	Contours of maximum shear strain for a fatigue crack grown at $\Delta K = 8.8 \text{ MPa}\sqrt{\text{m}}$ approaching particle $P_2$ , as shown in Fig. 6(e)	45
17	Strain distribution for the fatigue crack, shown in Fig. 9, grown at $\Delta K = 18.5 \text{ MPa}\sqrt{\text{m}}$ and having several non-connected microcracks	46
18	Strain distribution for a fatigue crack grown at $\Delta K = 19.5 \text{ MPa}\sqrt{\text{m}}$ having several non-connected microcracks	47
19	Crack opening displacements for the microcracks of Fig. 18	48
20	Distribution of maximum shear strain around the crack tip, shown in the inset, just prior to final fracture	49
21a-b	(a) Distribution of effective strain (normalized by the crack tip strain) ahead of the fatigue crack shown in Figs. 6(b) and 12; (b) Distribution of effective strain (normalized by the crack tip strain) perpendicular to the loading axis for the fatigue crack shown in Figs. 6(b) and 12	50
22a-b	(a) Distribution of effective strain (normalized by the crack tip strain) ahead of the crack shown in Figs. 10 and 20; (b) Distribution of effective strain (normalized by the crack tip strain) perpendicular to the loading axis for the fatigue crack shown in Figs. 10 and 20	52
23	Plastic zone sizes parallel to the loading axis for the composite compared to those for fatigue cracks in unreinforced 7075-T651	54
24	Alteration of the distribution of effective strain (normalized by the crack tip strain) ahead of the crack shown in Figs. 6(d) and 14(a) by the SiC particle	55
25	Distribution of effective strain along each side of SiC particle $P_2$ , shown in Figs. 6(e) and 16, going from left to right across the plane of the crack	56

## LIST OF FIGURES (continued)

- |    |   |    |
|----|---|----|
| 26 | Determination of crack closure from measured crack tip parameters and computed $\Delta K_{th}$                                    | 57 |
| 27 | Comparison of crack tip strains for the composite to those for unreinforced aluminum alloys showing the similarities in magnitude | 58 |



## THE EFFECT OF PARTICULATE SiC ON FATIGUE CRACK GROWTH AND FRACTURE TOUGHNESS OF A CAST-EXTRUDED ALUMINUM ALLOY COMPOSITE

David L. Davidson  
Southwest Research Institute  
San Antonio, Texas 78284

### ABSTRACT

A detailed micromechanics analysis has been performed on a composite of 2014 aluminum alloy matrix with 15 vol.% particulate SiC. This composite was manufactured by the Dural Co. by casting and extrusion. The matrix alloy was peak aged before testing. The microstructure was found to contain about 3% intermetallic particles in addition to those expected for this material. Fatigue cracks were grown from approximately threshold to rapid fracture stress intensities. Fatigue crack growth rates and fracture toughness were measured. Analyses of the crack tips were performed by stereoimaging at low and intermediate stress intensities, and just prior to the onset of rapid fracture. Detailed strain maps were derived, and considerable influence of SiC on strain was found. Analyses of microcracks near the main crack were made and found to have only a small influence on fracture. Fatigue threshold was explained on the basis of measured and calculated crack closure, but fracture toughness values measured could not be rationalized by fractography or by applying previously developed quantitative models.

### I. INTRODUCTION

The addition of silicon carbide particles to aluminum alloys results in an increased modulus, which may also be accompanied by an increased yield stress, depending on the alloy, heat treatment, and manufacturing method [1]. Other attributes for these composites may be enhanced resistance to wear [2], corrosion [3], and fatigue crack initiation [3], when compared to the matrix materials alone. Unfortunately, fracture toughness and fatigue crack growth resistance of these composites are usually inferior to the aluminum alloy matrix materials [4,5]. Why is the crack growth resistance of this class of composites inferior to aluminum alloys, and what can be done to enhance the composite fracture properties? The research reported here has used crack tip micromechanics, in addition to more traditional methods, to gain insight into the origins of the fracture characteristics of one of these materials.

Three manufacturing methods have been used for producing these composites: (1) silicon carbide are introduced into a molten bath of aluminum alloy, which is then cast and often further worked by extrusion or forging, and may be precipitation hardened, depending on the properties of the matrix alloy; (2) aluminum alloy powders are mixed with powdered silicon carbide which is subsequently consolidated into billets using powder metallurgy forming processes, and (3) silicon carbide particles are mechanically alloyed into aluminum alloy powders and then formed into billets using powder metallurgy consolidation techniques.

The author's research on the fatigue and fracture toughness of these composites has concentrated on the effects of matrix alloy type and heat treatment, particle size and volume fraction for manufacturing methods (1) and (3), as given above. Micromechanics has been used extensively in this and similar research to complement the more usual, macroscopic investigative techniques of fracture research. While the general fracture characteristics of these composites have been determined, and published [4,6], the work reported here is a detailed analysis of crack growth through a cast composite and complements similar, previously published work on composite manufactured by mechanical alloying [7].

## II. MATERIAL

The simplest and least expensive method for manufacturing aluminum matrix SiC composites is the addition of silicon carbide particles (grit) to molten aluminum alloys. The material investigated by this research was fabricated using this method in 1985 by Science Applications International of San Diego, CA, now called the Dural Aluminum Composites Company. Particulate SiC at a concentration of 15 % by volume was added to 2014 aluminum alloy (4.4Cu, 0.8Si, 0.8Mn, 0.4Mg in wt. %) using a proprietary method for dispersion. After casting, the material was subsequently extruded at 490°C, with a 8.2:1 ratio, to produce bars of 16 x 38 mm cross section. Upon receipt of the material, half of it was cut into pieces about 60 mm long, solutionized at 500°C for 2 hrs., precipitation aged to peak hardness (T6) at 160°C for 16 hrs., according to the recommendations of the manufacturer, which is not the standard age hardening treatment for unreinforced 2014 alloy. For comparison to other composites, this material was designated 2014 - PA + 15v/o SiC. This composite gave the highest value of fracture toughness

measured for the 13 variations in manufacturing technique, matrix alloy, SiC volume fraction, and heat treatment investigated [4], which is the reason a detailed micromechanics investigation of fracture was undertaken.

The microstructure of this composite was characterized by optical and electron microscopy, both scanning (SEM) and transmission (TEM). The level of dispersion uniformity may be judged from Fig. 1(a), a low magnification optical microscope photograph. The higher magnification secondary electron SEM photograph in Fig. 1(b) reveals the presence of much smaller particles. A backscattered micrograph, Fig. 1(c) suppresses visibility of the SiC particles and clearly shows that many of the small to intermediate size particles are not SiC. From energy dispersive x-ray analysis, these particles were found to be of two compositions: about 80% of the particles were rich in Al, Si, Fe, and Mn, and about 20 % of the particles were rich in copper.

The microstructure of the aluminum alloy matrix was further investigated by transmission electron microscopy of thin foils prepared by chemical jet polishing of dimpled blanks. The matrix structure, shown in Fig. 2, is reasonably typical of an aluminum alloy, except that dispersoid-free channels were found to be a fairly common feature. A complete analysis of the dispersoids seen in Fig. 2 was not made, but volume fraction ( $\approx 0.01$ ) and size range ( $0.05 - 0.25 \mu\text{m}$ ) are approximately those expected for aluminum alloys [8].

The size distribution of all particles was determined using a Tracor Northern Image analysis system. Six SEM photographs made at a magnification of 500 times were analyzed. The distribution of particle sizes is fairly broad, as shown in Fig. 3, and peaks at 5 to 7  $\mu\text{m}$ . Total areal fraction of particles, the integral of the curve in Fig. 3 converted to volume fraction, was found to be 18.5%, which is somewhat larger than the 15 v/o of SiC added during manufacture of this composite.

An analysis was also made of non-SiC particles which revealed a large number of very small particles, but also with a few larger particles, up to about 15  $\mu\text{m}$ . The total volume percent of the 2300 particles analyzed was found to be about 3.7%. If this fraction is subtracted from the overall particle volume, then SiC is approximately equal to the manufacturer's stated value.

The distribution of SiC particle size is approximately log-normal, with

a maximum at  $6.5\text{ }\mu\text{m}$ , as determined from plotting the data on a logarithmic-normal graph. This distribution is shown by the solid line in Fig. 3. The distribution departs from log-normal at small particle sizes due mainly to the presence of non-SiC particles.

### III. TENSILE AND FRACTURE PROPERTIES

Tensile stress-strain curves for the composite are shown in Fig. 4(a). Two tests were conducted, terminating in fracture strains of 0.016 and 0.024. From the tensile deformation curve, the cyclic stress-strain properties were estimated [9] by correlating stress to plastic strain, as shown in Fig. 4(b). The average values of measured and derived properties are shown in Table 1.

Fatigue crack growth rate curves are shown in Fig. 5. Two specimens of differing configuration and different testing techniques were used to generate these data. One method used a compact tension specimen, designated CT/CCFM, with outer dimensions of  $31 \times 32\text{ mm}$  by  $6.5\text{ mm}$  thick that was cycled in a computer controlled, servo-hydraulic laboratory fatigue machine which used a crack mouth compliance gauge to measure crack length. The crack was initiated by cycling at  $8\text{ MPa}\sqrt{\text{m}}$ ,  $R = 0.1$ ,  $10\text{ Hz}$ . Load was then decreased at the rate of  $1\text{ MPa}\sqrt{\text{m}}$  per mm of crack growth until a growth rate of about  $10^{-9}\text{ m/cycle}$  was achieved, then load was slightly increased and held constant and crack growth data were recorded.

Data for the second crack growth rate curve shown in Fig. 5 was derived from a single edge notched specimen, designated SEN/SEM,  $20\text{ mm}$  wide and  $3\text{ mm}$  thick which was machined to fit in a cyclic loading stage for the SEM [10] that was used for observations of the crack tip region under high resolution conditions. The crack was initiated from a  $0.5\text{ mm}$  wide slit approximately  $2.5\text{ mm}$  deep at  $\Delta K = 6\text{ MPa}\sqrt{\text{m}}$ ,  $R = 0.1$ ,  $10\text{ Hz}$ , in a laboratory servo-hydraulic fatigue machine. Crack length on both sides was monitored by periodically removing the specimen to an optical microscope. After crack initiation, the load was decreased until a crack growth rate of approximately  $10^{-9}\text{ m/cycle}$  was achieved, then periodically raised to obtain larger values of  $\Delta K$ . At several levels of  $\Delta K$ , the specimen was removed from the laboratory machine and inserted into the SEM cyclic loading stage for observation. The crack tip region was then photographed in the SEM at maximum and minimum load for further micromechanical measurements using the stereoimaging technique [11].

Fatigue cracks were allowed to grow to lengths which resulted in rapid fracture of the specimen, thereby allowing a fracture toughness value to be determined. Fracture surfaces were flat, evidencing no shear lips. Threshold values for fatigue crack growth,  $\Delta K_{th}$ , and values of fracture toughness,  $K_{IC}$ , measured by these methods are given in Table 1. The linear portion of each crack growth rate curve in Fig. 5 has been fit by the equation

$$da/dN = B\Delta K^S \quad (1)$$

Fitting constants for eq.(1) are listed in Table 1.

Reasons for the differences between the crack growth rate curves in Fig. 5 are unknown. Data collected for several other composites using exactly these same methods resulted in nearly duplicate curves, so it was concluded that these differences in fatigue crack growth properties represented differences in material, rather than differences in technique. The results of the SEN/SEM specimen match more closely those of other, similar composites; therefore, this curve was taken as being the most representative.

To study, in detail, interaction of the fatigue crack with SiC particles, the crack was grown in the SEM cyclic stage while being frequently monitored and photographed. A sequence of photographs made at  $\Delta K = 8.8 \text{ MPa}\sqrt{\text{m}}$  showing the progression of the crack through the composite is shown in Fig. 6. Clearly, the SiC particles are exerting a significant influence on the crack as the tip approaches them. Crack length versus the number of cycles is shown for this sequence in Fig. 7(a), while Fig. 7(b) gives matching growth rates. Crack tip positions in the photographs of Fig. 6 may be correlated with those in Fig. 7 by the letters designating the figure. At this level of  $\Delta K$ , only a single crack tip was observed, and no other microcracks near the main crack were found.

With increasing  $\Delta K$ , the crack tip behavior became increasingly more complex, and the effect of SiC on the crack tip changed. Typical behavior at intermediate levels of  $\Delta K$  is shown in Fig. 8. If the crack tip was relatively far from any SiC particles, multiple crack tips were often observed, Fig. 8(a), but when the crack tip grew to within close proximity of SiC particles, the crack tip tended to remain singular, Fig. 8(b). Reasons for this multiple matrix cracking are unknown, but it may have something to do with the dispersoid-free channels found in the matrix by TEM, Fig. 2(b).

At  $\Delta K = 19 \text{ MPa}\sqrt{\text{m}}$ , multiple cracks were often found to form in the vicinity of the main crack. This behavior is illustrated in Fig. 9, which shows the formation and evolution of the microcracks as the main crack grew. Microcracks formed both at the interfaces of SiC particles and in the matrix regions between particles.

As the stress intensity approached  $K_{IC}$ , the zone of microcracking near the main crack decreased, as illustrated in Fig. 10, although only one crack tip in this state was observed. Tearing occurred during the loading cycle of Fig. 10, and rapid fracture initiated on the next loading cycle. The extensive plasticity associated with this level of stress intensity necessitated examination at the low magnification shown.

Micromechanics analyses were made for the cracks shown in Figs. 6, 9 and 10, covering the range from near- $\Delta K_{th}$  to  $K_{IC}$ , and are shown in sections IV and V, following a discussion of the fracture surface examination.

### Fractography

Fracture surfaces of both the fatigue crack growth and overload regions were examined in the SEM. Evidence was sought for periodic crack arrest markings (striations) over the whole range of crack growth rates, but none was found. A typical fractograph at mid- $\Delta K$  range is shown in Fig. 11(a), where some isolated regions of periodic markings may be seen, but these striations (see inset) are quite different from those caused by fatigue crack growth through unreinforced alloys [12].

During examination of the surface created by fast fracture, regions of dimpled rupture were sought. If found, these regions might have indicated that fracture toughness was controlled principally by microvoid growth and coalescence. However, only small, isolated patches of dimples were found, a few of which are illustrated in Fig. 11(b). The broken and debonded SiC particles shown in the photograph should also be noted. Similar features were seen also on fast fracture surfaces of many other, similar composites, so they are not unique to this material. The roughness of the fracture surface, both that created by fatigue and fast fracture, was measured for possible correlation to either roughness induced fatigue crack closure or increased toughness due to crack tortuosity. The surface roughness did not correlate

with either the level of fatigue crack closure,  $\Delta K_{th}$  [6], nor  $K_{Ic}$ , the magnitude of fracture toughness measured [4]. In summary, fractographic examination provided no assistance in quantitatively assessing the mechanisms of fracture for this composite.

#### IV. MICROMECHANICS

The stereoimaging technique was used extensively to map the strain fields associated with the fatigue crack growth sequence shown in Figs. 6, 9 and 10, which are a progression of crack growth rates from near threshold to near fast fracture. The highest resolution stereoimaging measurements made to date were used to detail the interaction between the crack and SiC particles. Although extensive manipulation of the data was made using various analyses and computer graphics, the results shown have been limited to those most interesting.

##### Fatigue at Low $\Delta K$

The distribution of maximum shear strain around the fatigue crack tip shown in Fig. 6(b), which was relatively distant from SiC particles, is illustrated in Fig. 12. The distribution of strain surrounding this crack tip, as well as the crack opening displacement (inset), is very much like that found for fatigue cracks in unreinforced aluminum alloys [13]. Strain is a maximum at the crack tip and, as the contours of strain show, plasticity is more extensive ahead of the crack tip than to each side of it. The crack opening displacement parallel to the loading axis, COD<sub>x</sub>, varies as the square root of the distance behind the crack tip.

After the crack grew for some distance towards the whisker-like SiC particle in its path, designated  $P_1$  in Fig. 6(c), a very similar strain distribution is again found, when viewed on a coarse scale, Fig. 13(a), and the COD (inset) is similar to that already shown. However, when the strains are determined with higher resolution near the end of  $P_1$ , as shown in Fig. 13(b), it is clear that intense deformation has occurred there, and that the strain level in  $P_1$  has increased markedly.

A further increase in crack length, Fig. 6(d), causes the interaction between the crack and particle to intensify. At this point, the crack has begun

to deflect around  $P_1$ . The strain map in Fig. 14 indicates that severe strain localization has occurred ahead of the crack tip and along the interface with the particle, and the COD (inset) is likewise affected by this strain localization. Very large strains, predominantly shear in character, have developed in the central region of the SiC particle -- the effect is remarkable when visualized in the stereoviewer. Another way to interpret this interaction between the crack and  $P_1$  is to convert the strains of Fig. 14 to stresses. This computation was accomplished using the derived cyclic stress-strain curve, Table 1, for the aluminum alloy matrix [14], while stresses in the SiC particle were computed by combining the total effective strain and modulus for SiC. The distribution of effective stresses thus derived is shown in Fig. 15, where the field of view has been rotated counterclockwise with respect to the strain contour plot shown in Fig. 14. Note that the stress scale in Fig. 15 is logarithmic; therefore, stresses in the SiC particle are extremely large, and there is a very large stress gradient along the matrix/particle interface. This effect is much easier to show with the distribution of stress than using the distribution of strain.

The strains and stresses shown in Figs. 14 and 15 are actually the changes which occur on going from minimum to maximum load. Since the residual stress at a fatigue crack tip is in compression at minimum load, the stress change cannot be directly related to what is known about the strength of SiC. The maximum stress change in the particle was determined to be about 16 GPa, which is still only about 3% of the modulus, and is less than might be expected for the fracture strength of a whisker of perfect SiC of very short gauge length [15]. The rapid variation of stress across the interface shown in Fig. 15 illustrates very well the reason that the term "interfacial strength" is difficult to apply when considered on a micromechanics scale. Conversely, the toughness of the interface is a well-defined quantity which may be used as a measure of interface fracture resistance [16].

Further cycling of the specimen caused the fatigue crack to be deflected around the left end of the particle  $P_1$ , only to encounter the more rounded particle  $P_2$ , as shown in Fig. 6(e). The distribution of strain in Fig. 16 illustrates, again, that deformation in the matrix has been "channeled" by the presence of this particle, and that the strains within the particle are relatively large, but in this case not as large as in particle  $P_1$ . The effect of  $P_2$  on the



COD of the crack at this stage is not as great as was the effect of  $P_1$  on the crack tip in Fig. 14.

### Fatigue at Intermediate $\Delta K$

Contours of maximum shear strain surrounding the crack in Fig. 9(a) are shown in Fig. 17. Opening displacement of the main crack (inset) has been considerably altered in comparison to that of a crack at lower  $\Delta K$  which showed no microcracking, e.g., Fig. 12. The Mode I opening, COD<sub>x</sub>, is no longer linear in  $\sqrt{y}$ , and Mode I = Mode II up to 12  $\mu\text{m}$  behind the tip. Perturbation of the strain field in the crack tip region is not as evident in Fig. 17, as might be thought from the locations and opening displacements of the microcracks seen in the photograph, although the strains at the tips of the microcracks are clearly elevated. The strain contours show some differences between the regions of maximum strain and the tips of the microcracks on the photographs. This may be an indication that there is a difference between surface and subsurface crack tip locations.

Crack opening displacements for these microcracks were determined, and these were combined with the crack tip strains to estimate the  $\Delta K$  levels of these microcracks using the relation [17]

$$\Delta K = (E\Delta\sigma\delta)^{1/2} \quad (2)$$

where  $E$  = composite tensile modulus (108 GPa),  $\Delta\sigma$  = cyclic stress at the crack tip, calculated using the crack tip strain in the derived cyclic stress-strain curve, Table 1, and  $\delta$  = CTOD (defined as the COD<sub>x</sub> or COD<sub>y</sub> at the distance of 1  $\mu\text{m}$  behind the tip). Eq. (2) was used to compute a  $\Delta K_x$  and  $\Delta K_y$  for the x and y openings at both ends of a crack, and these were combined to give  $\Delta K_{eq} = (\Delta K_x^2 + \Delta K_y^2)^{1/2}$ . The  $\Delta K_{eq}$  at each end of the crack were then averaged to give one value for each microcrack. The results of these computations are given in Table 2, where it may be seen that  $\Delta K_{eq}$  decreases as  $\theta$  increases, as would be expected from the elastic stress distribution surrounding a crack tip. However, this change might also be attributed to the increase in distance of the microcrack from the main crack tip.

For the microcracks shown in Fig. 9(b), the strain contours are shown in Fig. 18, and the COD for the main crack is shown in the inset. COD values for the microcracks are shown in Fig. 19, where the level of Mode II opening, approximated by  $COD_y$ , may be seen to vary with angular location relative to the main crack. These microcracks have been analyzed in the same way as those for the previous case, and the results are shown in Table 2. Magnitude of  $\Delta K_{eq}$  again decreases as  $\theta$  increases, just as for the previous case, but for this crack tip, the distance from the main crack tip,  $r$ , is more constant than for the previous case.

The effect of the microcracks on the stress intensity factor for the main crack has been computed using the analysis of Rose [18]. The analysis for each microcrack is independent of the other microcracks, but this assumption is reasonably valid because of the spacing of the microcracks. The results of this analysis, given in the last column of Table 2, indicate that the microcracks are not having much of an effect on the main crack, with the maximum elevation in the  $K_I$  of the main crack of 3%. The low level of this effect is due to the considerable distance between the main crack tip and the nearest microcrack (8  $\mu\text{m}$ ).

Crack opening displacements and crack tip strains of the main crack shown accompanying each figure have been used to compute a  $\Delta K_{eq}$ , the local driving force, using the same method as described above for the microcracks. The results of these computations are shown in Table 3. For each of these crack tips,  $\Delta K_{eq}$  is smaller than the applied  $\Delta K$ ; the difference is due to fatigue crack closure. Similar results have been shown for several other materials [19], including aluminum alloys.

The magnitudes of  $\Delta K_{eq}$  for microcracks are considerably less than  $\Delta K_{eq}$  for the main crack. This correlates well with the observation that the microcracks grew only a small amount as the main crack moved past them, and that the maximum amount of observed growth was for microcrack 1, that closest to the path of the main crack.

### Approach to $K_c$

The distribution of maximum shear strain is shown in Fig. 20 for the tearing crack of Fig. 10. This strain distribution is different than for a fatigue crack at lower  $\Delta K$  in that there is considerable strain along the flanks of the crack and the strain ahead of the crack tip is more pronounced. The maximum strain is much larger than that found for other, similar composites, although it is not exactly at the crack tip, but 5  $\mu\text{m}$  behind it, consistent with the shape of the crack tip. The COD (inset) also evidences unusual behavior as compared to crack tips at lower  $\Delta K$ , but it is not blunt like that shown in Fig. 18. These differences are probably the result of crack tearing and the loss of constraint on the surface caused by the large plastic zone which has developed at this high  $K$  level. The strain distribution is consistent with development of a slant fracture mode, but fractography did not evidence any well-developed shear lip, so the effect, if present, was small or local.

### V. STRAIN DISTRIBUTIONS AND PLASTIC ZONE SIZES

The distributions of strain within the plastic zones of the fatigue cracks on which micromechanics analysis was performed have been studied in detail. The main purpose of this analysis was to compare the effects of SiC in this composite with a similar, unreinforced aluminum alloy. Effective total strain range (normalized by the crack tip strain)  $\Delta\epsilon'$ , within the plastic zones directly ahead of the crack tip (along the y-axis) and in the loading direction ( $\pm x$ -axes) were matched against two distribution functions previously used for strain analyses [20]:

$$\Delta\epsilon' = A' + M' \ln(B+r) \quad (3)$$

$$\text{and} \quad \Delta\epsilon' = A'/(B+r)^m \quad (4)$$

where  $r$  = distance from the crack tip along either  $y$  or  $\pm x$ ,  $A'$ ,  $M'$  and  $B$  are fitting constants, and  $m = 1/(n+1)$  ( $n$  = work hardening coefficient, Table 1).

Strain distributions parallel and perpendicular to the loading axis are shown in Figs. 21 and 22 for the lowest and highest  $\Delta K$  values applied. For the

low and intermediate levels of  $\Delta K$ , the logarithmic function, eq. (3), fit the strain distribution better than eq. (4). As seen in Fig. 21, the fit to the data, which includes the crack tip strain, is good, particularly ahead of the crack tip. The ordinate of these graphs is the strain normalized by the crack tip strain. This result is consistent with the analysis of a much larger data base of strain distributions ahead of cracks in a variety of alloys [20]. For the distributions of strain in the loading axes ( $\pm x$ ), the fit is not as good because of scatter in the strains. However, if all the data available at the lower values of  $\Delta K$  are considered, eq.(3) describes these data somewhat better than eq. (4). This is contrary to the strain distribution given by another aluminum alloy - SiC composite studied earlier [7]. It must be noted, however, that eqs. (3) and (4) are very similar within the plastic zone; the differences in these functions only occur at large  $r$  where little strain data exists. Thus, using either strain distribution function results in computed values of plastic zone size which are nearly equal.

At the largest  $\Delta K$ , eq.(3) again fits the data better than eq.(4), although scatter in the data in the loading directions ( $\pm x$ ) again lowers confidence in this conclusion. The fits obtained are shown in Fig. 22. One of the reasons that the logarithmic function is considered to fit better than the exponential is that the values of  $m$  in eq. (4) which best fit the data are  $\approx 1.3$ , whereas,  $m \approx 0.9$  when determined from work hardening coefficient.

Values of the constants derived for a fit of the strain data to eq. (3) are given in Table 4, together with the derived plastic zone size (PZS) parallel and perpendicular to the loading axis. The table does not include those data derived when the crack tip was interacting strongly with SiC particles; they are examined separately. The definition of elastic strain used in deriving the PZS values given in Table 4 is twice the elastic strain at 0.2% offset yield, which for this composite is 0.0108. Thus, strain at the defined PZ boundary is equivalent to the cyclic yield strain. This definition is consistent with the strains, which were determined between minimum and maximum load. If PZ boundary is defined as the proportional limit or the monotonic yield strain, then values of PZS are increased from 20 to 40%. The last column of Table 4 lists the ratio of the PZS ahead of the crack tip to the size perpendicular to that. This ratio is consistently about 1.7, except for the K level just below fast fracture.

A similar analysis of crack tip strain distributions was performed on fatigue cracks in 7075-T651 [20]. Plastic zone sizes parallel to the loading axis, defined in the same way as for this composite, are compared in Fig. 23. Even though 7075 has a higher yield strength ( $\approx 500$  MPa) than this composite, the PZS is larger at lower  $\Delta K$  values. This indicates that yield stress cannot be used as a valid normalizing parameter.

At lower values of  $\Delta K$ , presence of the SiC particles near the crack tip can affect the strain distribution markedly. The strain distribution directly ahead of the crack shown in Fig. 14 is plotted in Fig. 24. If the strains at the crack tip and farthest from it are taken together, as indicated by the line, then the distribution function is again that of eq. (3), with constants comparable to those shown in Table 4 ( $A' = 1$ ,  $M' = -0.382$ ,  $B = 1$ ). It is obvious that strains within the SiC particle and between the crack tip and the particle are much lower. Effective strain at the crack tip ( $\Delta\epsilon(0) = 0.24$ ) is amplified by a factor of 3 relative to the other crack tips analyzed at this same  $\Delta K$  ( $\Delta\epsilon(0) \approx 0.07$ ). This is caused by the concentration of shear strain in the region between the crack tip and the SiC particle. The plastic zone ahead of this crack tip extends to  $11\text{ }\mu\text{m}$  compared to  $\approx 26\text{ }\mu\text{m}$  for the other crack tips analyzed at this same  $\Delta K$  (Table 4). Thus, the effect of the SiC particle has been to amplify the strain at the crack tip, while decreasing the plastic zone size.

The effect of deformation near the crack tip on the interfacial strains is indicated in Fig. 25 which plots the strain on each side of the large SiC particle shown in Fig. 16. The abscissa of Fig. 25 is the distance along the interface from left to right, with the plane of the crack shown for reference. Clearly, strains in the matrix are larger, and there is high gradient of strain across the interface. But even with the resolution of the measurements made here, it is not possible to determine if the crack will grow exactly in the interface or a few Angstroms into the matrix. The crack did, in fact, advance to the right around this particle within the next few cycles, and it could not be determined, even from observations at 8,000X, whether or not the crack advanced exactly through the interface.

## VI. DISCUSSION

The objective of this research has been to gain an overall understanding of fracture in this composite, and specifically to ascertain the effect of SiC particulate on fracture processes. This presupposes a depth of understanding

of fracture processes which, in fact, does not exist. It is clear enough that plasticity of the matrix alloy within the plastic zone of a crack is principally responsible for the fracture characteristics of the composite, and that one of the main effects of the SiC particulate is to modify the plastic response of the matrix alloy.

### Fatigue:

This composite exhibits a  $\Delta K_{th}$  for fatigue crack growth similar to unreinforced alloys. As has been demonstrated [19], this is an expression of the effects of fatigue crack closure, and is directly linked. A model has been advanced [19] which links the slip characteristics of the material with the magnitude of  $\Delta K_{th}$ . The model assumes that crack growth cannot occur when dislocations cannot be emitted from the crack tip. Crack growth ceases to occur when the stress at the tip of a slip line of length  $r_s$  emanating from the crack tip is reduced to the yield value,  $\sigma_y$ . An approximation to this condition is given by

$$\Delta K_{th} = \sigma_y \sqrt{2\pi r_s} \quad (5)$$

For a particulate reinforced composite, the model assumes that the limiting slip distance is equal to the mean free path of dislocations, which may be computed from [21]

$$r_s = (2d/3)[(1-v_f)/v_f] \quad (6)$$

where  $v_f$  = the volume fraction and  $d$  = the diameter of the SiC. Unfortunately, from the modeling viewpoint, there is a spread in size and volume fraction of SiC particles, which makes computation of  $r_s$  difficult. As an approximation, it has been assumed that  $d = 6.6 \mu\text{m}$ , the most probable size of particle, and that all 15% SiC is of this size. Therefore, from eq. (6),  $r_s = 25 \mu\text{m}$ . Using this value in eq. (5) gives  $\Delta K_{th} = 4.4 \text{ MPa}\sqrt{\text{m}}$ , which is below those values measured by fatigue crack growth, as listed in Table 1. Considering the variation in measured  $\Delta K_{th}$  and the approximations made in the above computations, the agreement between measured and computed values is fairly good.

The level of Mode I crack closure is set by the magnitude of  $\Delta K_{th}$ , which means the level of  $\Delta K_{eff}$  at any value of  $\Delta K$  is found from

$$\Delta K_{eff} = \Delta K - \Delta K_{th} \quad (6)$$

Evidence for the validity of eq. (6) is presented in Fig. 26, which shows a relationship similar to that previously derived for unreinforced 7075-T651 and 7091 [19] aluminum alloys. The line drawn on the figure is from eq.(6). Data variation is due mainly to the crack response from cycle to cycle during crack growth; measurement accuracy is much better than the variation observed. The data used in this figure are from Table 3. It must be concluded from this analysis that an average level of fatigue crack closure at any  $\Delta K$  can be predicted, with reasonable accuracy, for this class of composites.

The plastic zone sizes shown in Fig. 23 indicate that crack tip plasticity is restricted by the presence of SiC particles, especially as the size of the plastic zone increases with  $\Delta K$  to envelop more particles. Further evidence of restricted plasticity was given by the strain distributions, e.g., Fig. 24. A comparison of crack tip strains for this composite with those of the aluminum alloys 7075 and 7091, Fig. 27, indicates that presence of the SiC has virtually no effect on crack tip strain, at least at low to intermediate  $\Delta K$ . It must be concluded that the main effect of the SiC is to restrict slip within the plastic zone, thereby decreasing plastic zone size, but without altering the functional form of the strain distribution.

Detailed examination of the interaction of a fatigue crack with SiC has shown that the crack is deflected by particles blocking the path of the crack, Figs. 6 and 7(a), but that crack growth rate is altered only over relatively small distances and by less than a factor of 10, Fig. 7(b). The SiC also altered the distribution of strain within the plastic zone, but not strain at the crack tip, unless the tip was very close to a particle. Again, this implies that crack growth rate is linked mainly to crack tip strain, and that deformation within the plastic zone occurs in response to the crack tip strain and is of little relevance to determining crack growth rate. There is good evidence, however, that deformation within the plastic zone controls the level of crack closure. Thus, the relationship between crack growth rate and  $\Delta K_{eff}$  is altered by the presence of SiC through the level of crack closure.

Particles of SiC near fatigue cracks have the effect of concentrating the strain in the region near the crack tip, e.g., Fig. 14. Very large stresses within the SiC particles result, but the SiC rarely breaks due to the constraints of surrounding material, and, apparently, the small size of the inherent flaws within the SiC. Thus, breakage of SiC is observed to occur mainly for larger particles [7].

Deformation within the matrix limits the magnitude of stress, but, due to continuity of deformation across the interface into the SiC particles, the stresses are very high in particles close to the crack. This results in a very large stress gradient across the interface and makes it difficult to define a stress at which particle/matrix debonding occurs. It is not clear, for this composite, that interfacial debonding occurs; rather, it appears as though failure usually occurs in the matrix within a micrometer of the interface. The exception to this occurs when several SiC are clumped together. This condition, illustrated in Figs. 17 and 18, can cause microcracking in the matrix/particle interface. This occurs, presumably, because of inadequate wetting or deformation in the fabrication process. The difficulty of defining a "bond strength" at the interface between the two parts of a composite, when viewed on a microscale, is certainly an opportunity for further thought and analysis.

#### Fracture Toughness:

Measured fracture toughness of this composite is 24 to 27 MPa $\sqrt{m}$ , which is higher than the 13 to 16 value measured for most of the other cast and extruded materials tested. The main reason this composite was chosen for detailed study was to determine the reasons for this relatively large value of fracture toughness. Fracture surface roughness has been proposed [22] as being proportional to fracture toughness, so this concept was examined for all the composites tested. A qualitative assessment of fracture surface cross sections revealed no relationship between these two variables, so it was not surprising that quantitative determination of the fracture surface roughness factor, which is related to the fractal dimension of the fracture surface profile, was also unrelated to measured fracture toughness [4].

In research on another composite, the factors contributing to fracture toughness were analysed and modeled [7]. For materials which form very few microvoids in the process of final fracture, the work expended in formation of



the crack tip plastic zone is the principal contribution to fracture toughness. For the composite studied here, very little evidence of microvoid formation was found from fracture surface examination, Fig. 11. Therefore, the model developed previously was used to compute fracture toughness. Strain measured at the crack tip for the cycle just prior to the onset of rapid fracture and the strain distribution parallel to the loading axis, Fig. 22(b), were used in the computation. The magnitude of fracture toughness computed by this procedure was 9 MPa√m, which is a factor of almost 3 smaller than that measured. This result implies that the model was formulated incorrectly or the measurements were inaccurate, or both.

The model was reviewed, but no problems were found. Variables which go into the model were, therefore, altered systematically until a value of  $K_{IC}$  approximating that measured was computed. To obtain a value of  $K_{IC} = 27$  MPa√m, the area under the stress-strain curve would have to be increased by 30% for any given strain, the unloading correction would have to be ignored, and the strain at the crack tip would have to be approximately twice that measured. These values are at such wide variance with the measured values that inaccuracies in measurement cannot be considered as the reason for the inability of the model to rationalize the results.

An estimate of  $K_{IC}$  may be made using the relation [23]

$$K_{IC} = (E\delta\sigma_y)^{1/2} \quad (7)$$

where  $\delta$  = CTOD and  $\sigma_y$  = yield stress. Using the value of CTOD measured, as shown in Fig. 20 (1.8 μm) gives  $K_{IC} = 11.7$  MPa√m, which agrees much closer to the result using the model than it does to the measured value. For  $K_{IC} = 25$  MPa√m, the CTOD would have to be 8.5 μm, which is almost 5 times that measured and well outside of any error in measurement. However, when this equation was used to compute  $K_{IC}$  for a similar composite, the result was again lower than that measured, but the difference was less [7].

It must be concluded from the above analyses that either the measurements of  $K_{IC}$  are incorrect, or the models are wrong. However, a thorough examination of both model and experimental results has not revealed

the reason for disagreement. Thus, the reason for the high fracture toughness of this composite remains unknown. The large variability of  $K_{IC}$  between specimens does bring into question whether the results obtained for  $K_{IC}$  (from two specimens) are typical, and whether the crack tip plasticity results (from one specimen) are typical. It is possible that the variance between test and model results is due to variations in material properties between samples, but the differences are so large as to question this explanation.

## VII. SUMMARY AND CONCLUSIONS

A detailed micromechanics analysis has been performed on the fracture characteristics of the aluminum alloy 2014, in peak aged condition, reinforced by approximately 15 v/o SiC particles averaging 6.5  $\mu\text{m}$  in diameter. This composite was manufactured by casting from the melt followed by extrusion.

1. The yield stress of the composite (345 MPa) was found to be lower than that of the base aluminum alloy (415 MPa). The matrix material was found to be inhomogeneous, with relatively large intermetallic particles widely distributed in the matrix. Transmission electron microscopy revealed the dispersoids expected in this alloy, but with some dispersoid-free regions not associated with the reinforcing particulate.

2. Fatigue cracks growing at low  $\Delta K$  have crack tip plasticity relatively unaltered by the reinforcing SiC, except that the plastic zone size is reduced. Cracks growing at higher  $\Delta K$  have their plastic zone deformation significantly altered by SiC particles, due mainly to the larger plastic zone which encompasses more particles. However, crack tip strains are not greatly changed by the presence of the SiC.

3. Crack closure measurements indicate a trend similar to that found for unreinforced material, but with a shifted level of closure. The threshold for fatigue crack growth, which is the same as the level of closure, may be computed from a knowledge of the SiC particle size and volume fraction. Crack surface roughness appears to have little influence on crack closure.

4. Strains in SiC particles within crack tip plastic zones were found to be high, with the accompanying high stresses. This causes a very large stress gradient at the particle/matrix interface which makes it difficult to define a debonding stress.

5. Microcracks separated from the main crack were formed within the plastic zone of fatigue cracks growing at intermediate  $\Delta K$ . These microcracks, which usually formed within clumps of SiC particles, were found to have little effect on the crack growth rate of the main crack because of their small number and relatively large distance from the main crack tip.

6. The fracture toughness measured for this material was found to be higher than that of similar composites having other matrix alloys. The reasons for this elevated toughness were sought by fractography and by comparison with a model for fracture toughness which is related to the work expended in formation of a plastic zone. No evidence for extensive formation of microvoids was found from fractography, and the model predicted that the  $K_{IC}$  would be approximately one-third of that measured. No rationalization of the measured  $K_{IC}$  could be made on the basis of plasticity. It may be that the values of  $K_{IC}$  measured are atypical.

#### ACKNOWLEDGEMENTS

This research was supported by The Office of Naval Research, contract N00014-85-C-206, Dr. S.J. Fishman, Project Monitor. The particle analyses and stereoimaging data reduction were performed by Jim Spencer, and the fatigue crack and material mechanical characterizations were performed by John Campbell. Transmission electron microscopy was done by Harold Saldana and Dr. Richard Page. Dr. K.S. Chan computed the effect of microcracks on the stress intensity of the main crack. The author is grateful to all of his colleagues for their skillful assistance with this research.

#### REFERENCES

1. S.V. Nair, J.K. Tien, and R.C. Bates: *International Metals Reviews*, 1985, vol. 30, pp. 275-290.
2. C. Milliere and M. Suery: *Mater. Sci. and Technol.*, 1988, vol. 4, pp. 41-51.
3. D.F. Hasson, C.R. Crowe, J.S. Ahearn and D.C. Cooke: *Failure Mechanisms in High Performance Materials*, Cambridge Univ. Press, Cambridge, 1985, p. 147-156.
4. D.L. Davidson: "Fracture Surface Roughness as a Gauge of Fracture Toughness: Aluminum-Particulate SiC Composites," *J. Mater. Sci.* (in press).
5. R.D. Goolsby and L.K. Austin: *Proceedings ICF-7* (in press).

6. D.L. Davidson: "The Growth of Fatigue Cracks Through Particulate SiC Reinforced Aluminum Alloys," *Engineering Fracture Mechanics* (in press).
7. D.L. Davidson: *Metall. Trans. A*, 1987, vol. 18A, pp. 2115-2128.
8. V.W.C. Kuo and E.A. Starke, Jr: *High Strength Powder Metallurgy Aluminum Alloys*, M.J. Koczak and G.J. Hildeman, eds., TMS-AIME, 1982, pp. 41-62.
9. J. Morrow: *Internal Friction, Damping, and Cyclic Plasticity*, ASTM STP-378, ASTM, Philadelphia, PA, 1964, pp. 45-81.
10. D.L. Davidson and A. Nagy: *J. Physics E.*, 1978, vol. 11, pp. 207-210.
11. D.R. Williams, D.L. Davidson and J. Lankford: *Exper. Mechanics*, 1980, vol. 20, pp. 134-139.
12. Metals Handbook, *Fractography and atlas of fractographs*, vol. 9, American Society for Metals, Metals Park, OH, 1974, pp. 64-78.
13. D.L. Davidson and J. Lankford: *Fatigue Mechanisms: ASTM STP 811*, ASTM, Philadelphia, PA, 1983, pp. 371-399.
14. Metals Handbook, *Properties and selection*, vol.1, American Society for Metals, Metals Park, OH, 1974, pp. 937.
15. F.D. Gac, J.V. Milewski, J.J. Petrovic and P.D. Shalek: "Silicon carbide whisker reinforced glass and ceramics," *Proceedings of the Conference on Composite Materials*, Cocoa Beach, FL, January 1984, pp. 53-64.
16. K.S. Chan and D.L. Davidson: "Driving Force for Composite Interface Fatigue Cracks," *Engineering Fracture Mechanics* (in press).
17. S.J. Hudak and K.S. Chan: *Small Fatigue Cracks*, R.O. Ritchie and J. Lankford, eds., TMS-AIME, Warrendale, PA, 1986, pp. 379-406.
18. L.R.F. Rose: *Inter. J. of Fracture*, 1986, vol. 31, pp. 233-242.
19. D.L. Davidson: *Acta Metallurgica*, 1988, vol.36, pp. 2275-2282.
20. D.L. Davidson: *Engineering Fracture Mechanics*, 1986, vol. 25, pp. 123-132.
21. J.W. Martin: *Micromechanisms in Particle-Hardened Alloys*, Cambridge Univ. Press, 1980, p. 43.
22. B.B. Mandelbrot, D.E. Passoja and A.J. Paullay, *Nature*, 1984, vol. 308, 721.
23. J.R. Rice and M.A. Johnson: *Inelastic Behavior of Solids*, McGraw Hill, New York, NY, 1970, pp. 641-72.

## TABLES

TABLE 1

## 2014-PA+15v/o SiC Mechanical and Fracture Properties

Tensile:

<u>Property</u>	<u>Units</u>	<u>Test 1</u>	<u>Test 2</u>
Young's Modulus	GPa	107	108
Proportional limit	MPa	260	210
0.2% offset Yield stress	MPa	342	346
Strain to fracture	%	1.6	2.4
$\Delta\sigma = \sigma_o \varepsilon_p^n$ : $\sigma_o$	MPa	678	842
$n$		0.111	0.158
Ultimate stress	MPa	450	468

Fatigue:

		<u>SEM</u>	<u>CT</u>
$\Delta K_{th}$	MPa $\sqrt{m}$	5.5	10
$da/dN = B\Delta K^S$ : B	m/cycle	$2.1 \times 10^{-12}$	$3.6 \times 10^{-12}$
$s$		5.5	4

Fracture Toughness:

		<u>Spec. 1</u>	<u>Spec. 2</u>
$K_C$	MPa $\sqrt{m}$	27.0	23.8

TABLE 2

$\Delta K$	Crack No.	r	l	Microcrack Analysis			$K_{eq}$	$K_I/K$ Main Crack
				$\theta$	Max. COD			
				x	y			
MPa $\sqrt{m}$		$\mu m$	$\mu m$	$^\circ$	-- $\mu m$ --		MPa $\sqrt{m}$	
18.5	1	12	8	24	0.24	0.20	4.4	1.03
	2	30	10	53	0.70	0.08	3.4	1.01
	3	36	14	78	0.37	0.06	3.1	0.99
19.5	1	23	14	20	0.84	0.62	6.2	1.02
	2	30	16	59	0.76	0.15	4.3	1.02
	3	35	20	107	0.13	0.10	2.2	0.97

TABLE 3

## Crack Driving Force Analysis

$\Delta K$	COD		Crack Tip strain	$\Delta\sigma$	Stress Intensity Factors			
	Mode I	Mode II			$\Delta K_I$	$\Delta K_{II}$	$\Delta K_{eq}$	$\Delta K_{eq}/\Delta K$
MPa $\sqrt{m}$	---- $\mu m$ ----			MPa	-----MPa $\sqrt{m}$ -----			
8.8	0.27	0.18	0.070	460	3.6	3.0	4.7	0.54
8.8	0.20	0.06	0.144	523	3.3	1.8	3.8	0.43
8.8	0.22	0.06	0.244	570	3.7	1.9	4.1	0.47
8.8	0.20	0.07	0.111	500	3.3	1.9	3.8	0.43
18.5	0.49	0.69	0.165	520	5.2	6.2	8.1	0.44
18.5	0.76	0.85	0.20	550	6.7	7.1	9.7	0.52
19.5	2.65	1.90	0.49	638	13.5	11.4	17.7	0.91
24.0	2.60	1.50	0.72	678	13.7	10.4	17.2	0.72

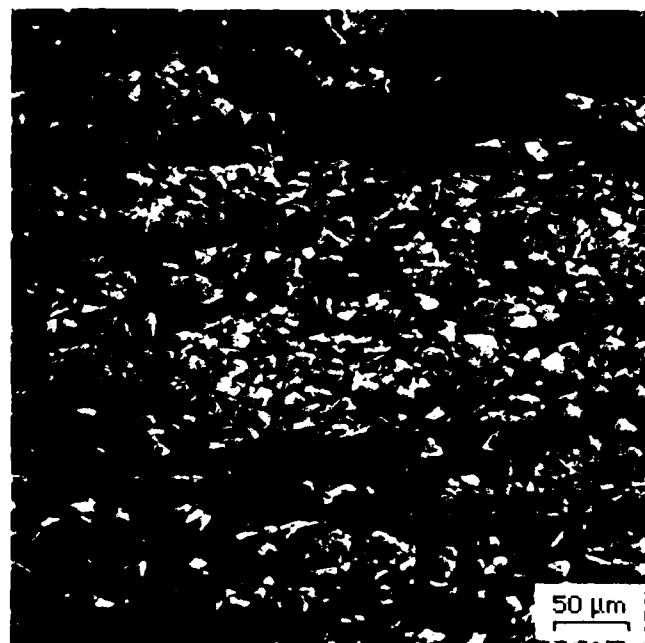


TABLE 4

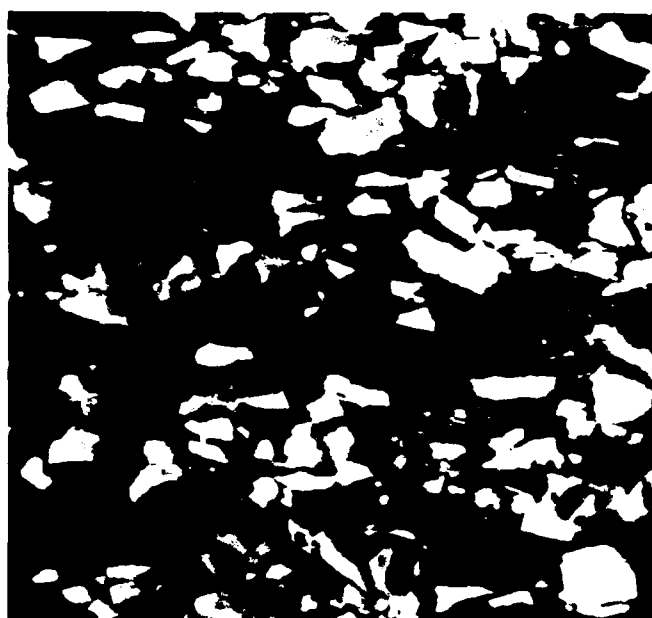
## Strain Distributions and Plastic Zone Size

Kmax MPa $\sqrt{m}$	Direc- tion	$\Delta\epsilon(0)$	A'	m	B $\mu m$	PZS $\mu m$	Ratio (y/x)	Calculated PZS ( $\mu m$ )
9.8	y	0.07	1.22	-0.313	2	27.8	1.49	16
	$\pm x$	0.07	1.26	-0.375	2	18.7		23
9.8	y	0.07	1.23	-0.327	2	24.8	1.65	16
	$\pm x$	0.07	1.27	-0.394	2	15.0		23
21.7	y	0.30	1.22	-0.320	2	38.4	1.65	81
	$\pm$	0.30	1.49	-0.445	3	23.2		113
29.5	y	0.34	1.0	-0.165	1	352	3.55	150
	$\pm x$	0.34	1.17	-0.247	2	99.2		208

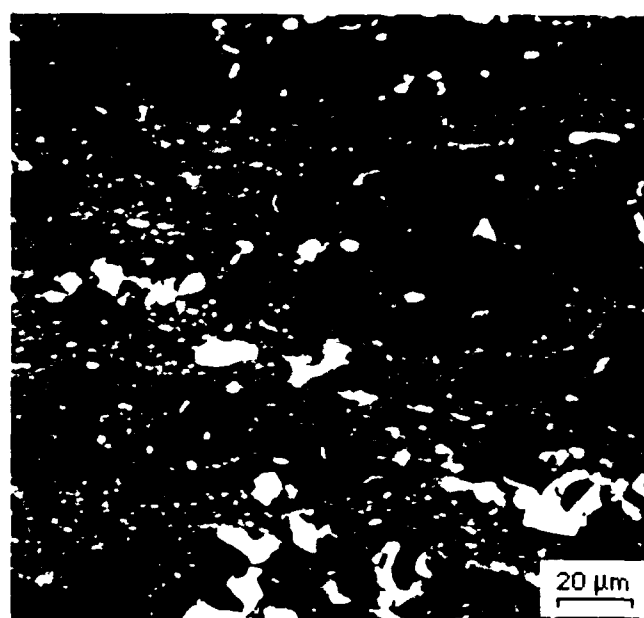
## F I G U R E S



(a)



(b)



(c)

Fig. 1 Microstructure of 2014 +15 v/o SiC. (a) Low magnification secondary electron image showing dispersion of SiC in matrix, (b) similar image at higher magnification showing particle shape and size, and (c) same area as in (b) by backscattered electron imaging showing the large number of intermetallic particles in the matrix.

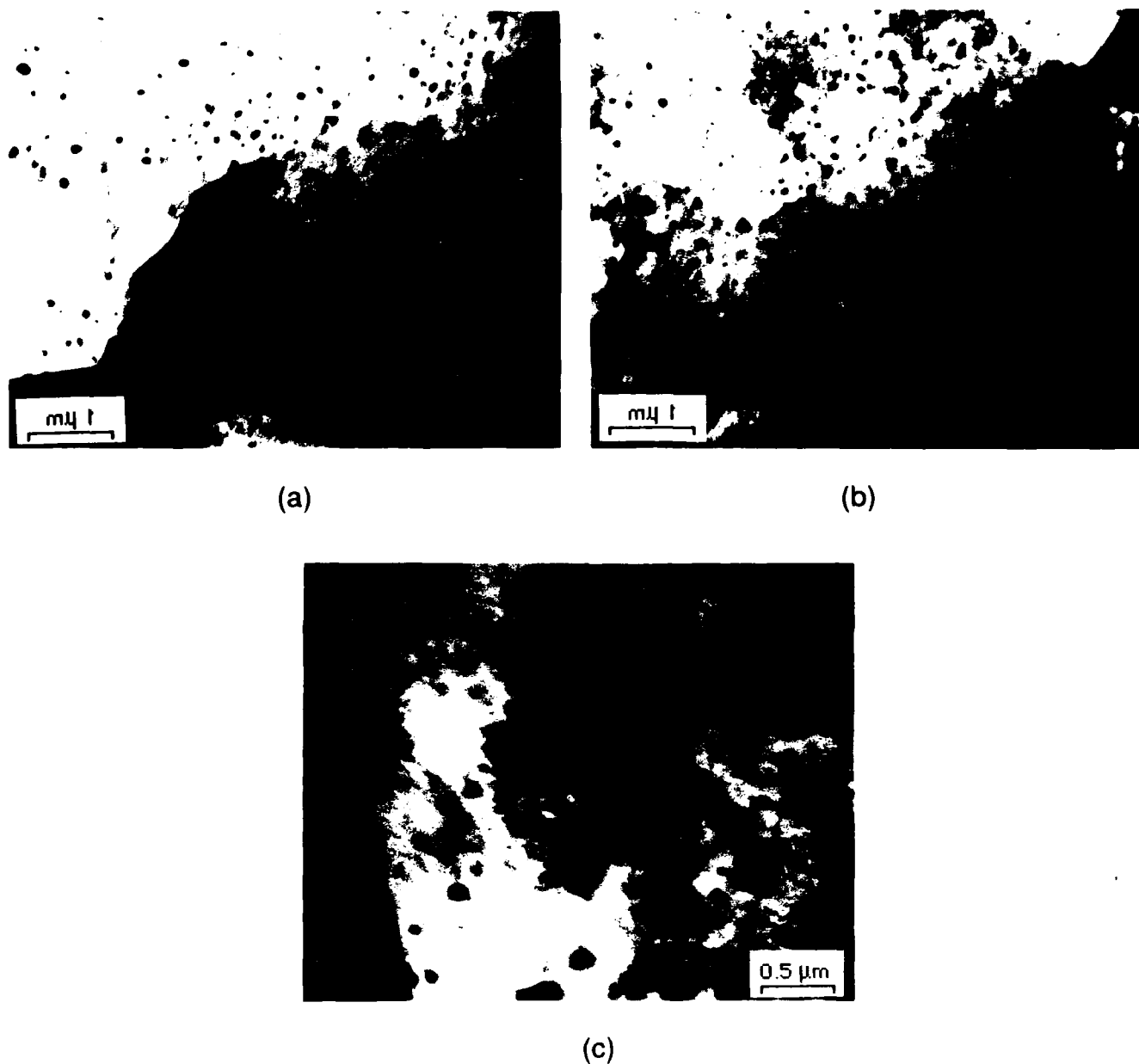


Fig. 2 Transmission electron microscopy of 2014-PA+15v/o SiC.  
(a) Some portions of the matrix exhibited subgrain formation, as illustrated here. A uniform distribution of dispersoids are also shown.  
(b) This micrograph shows one of the regions or "channels" free of dispersoids. (c) The interface between matrix and SiC particle (on left) shows no change in dispersoid distribution near the interface.

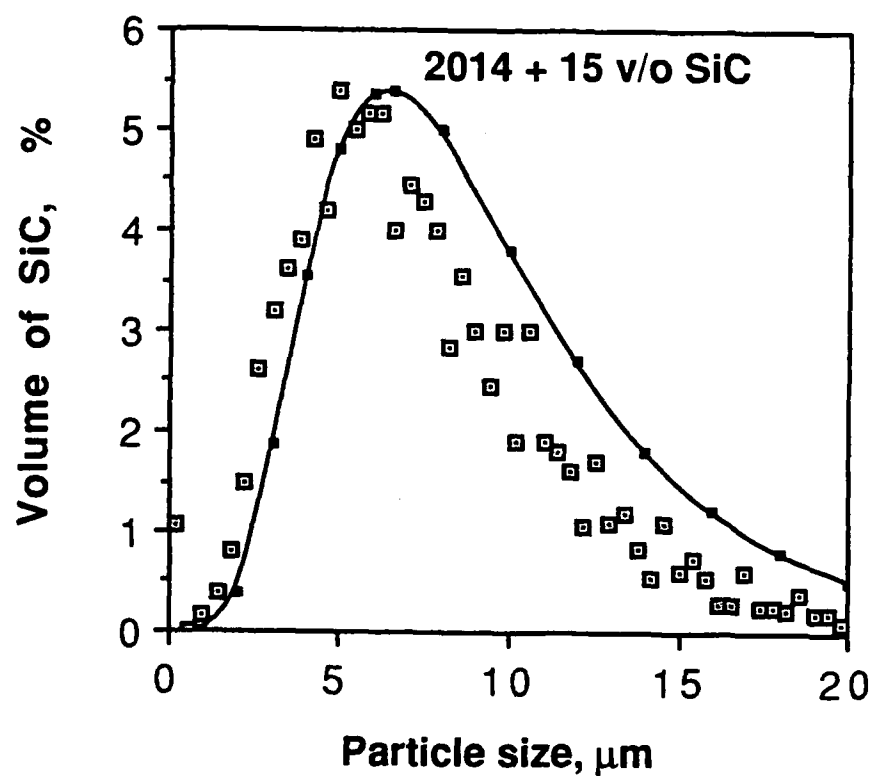


Fig. 3 Measured distribution of SiC and intermetallic particles in 2014-PA +15v/o SiC. The function fit to the data shows that the distribution is approximately log-normal.

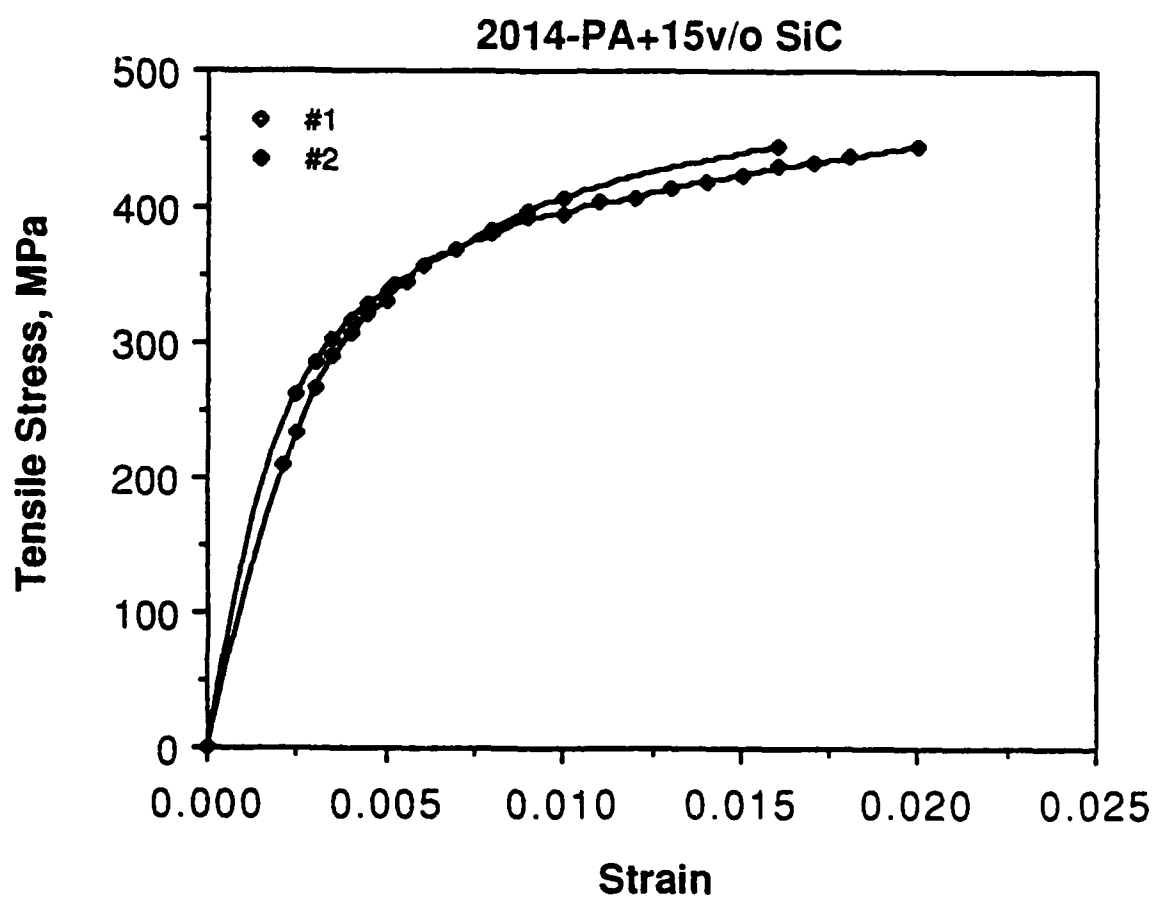


Fig 4(a) Stress-strain characteristics of two composite tensile specimens.

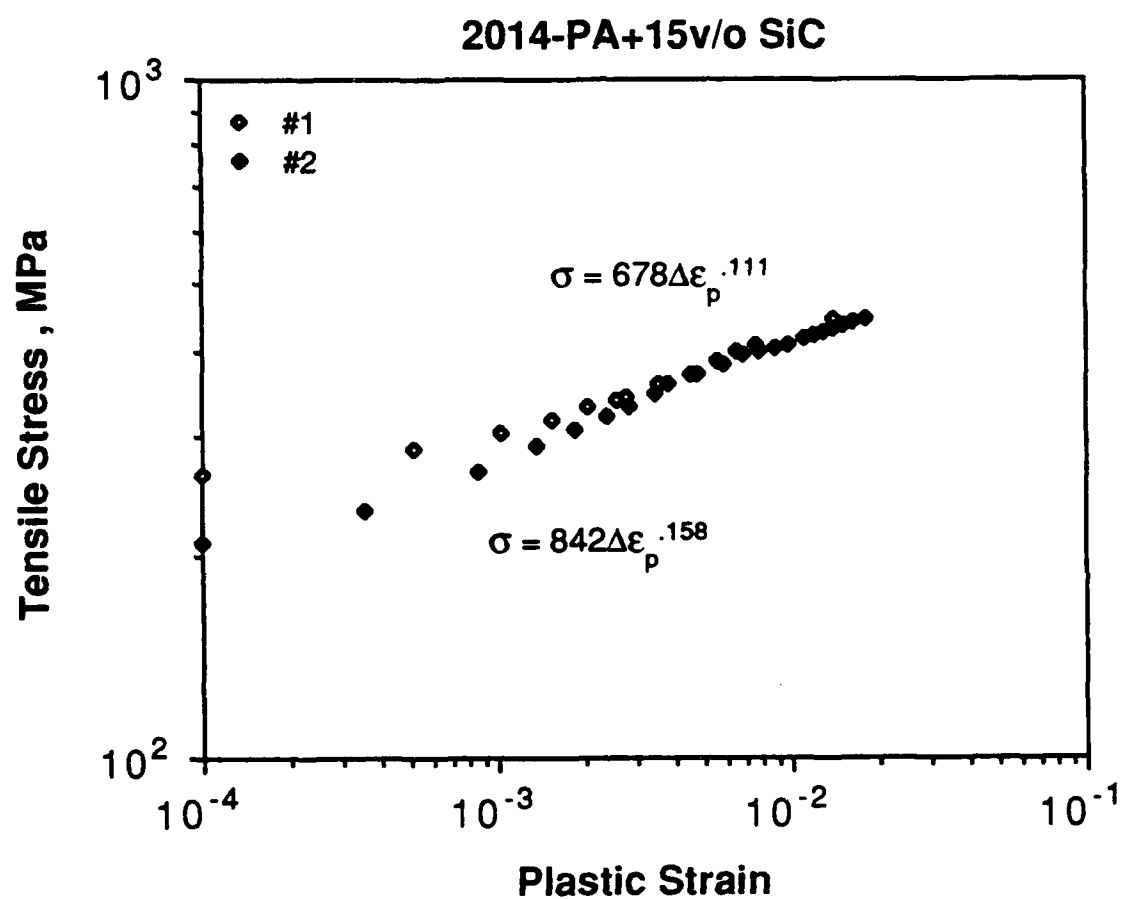


Fig. 4(b) Stress-plastic strain curves for two specimens of the composite derived from Fig. 4(a).

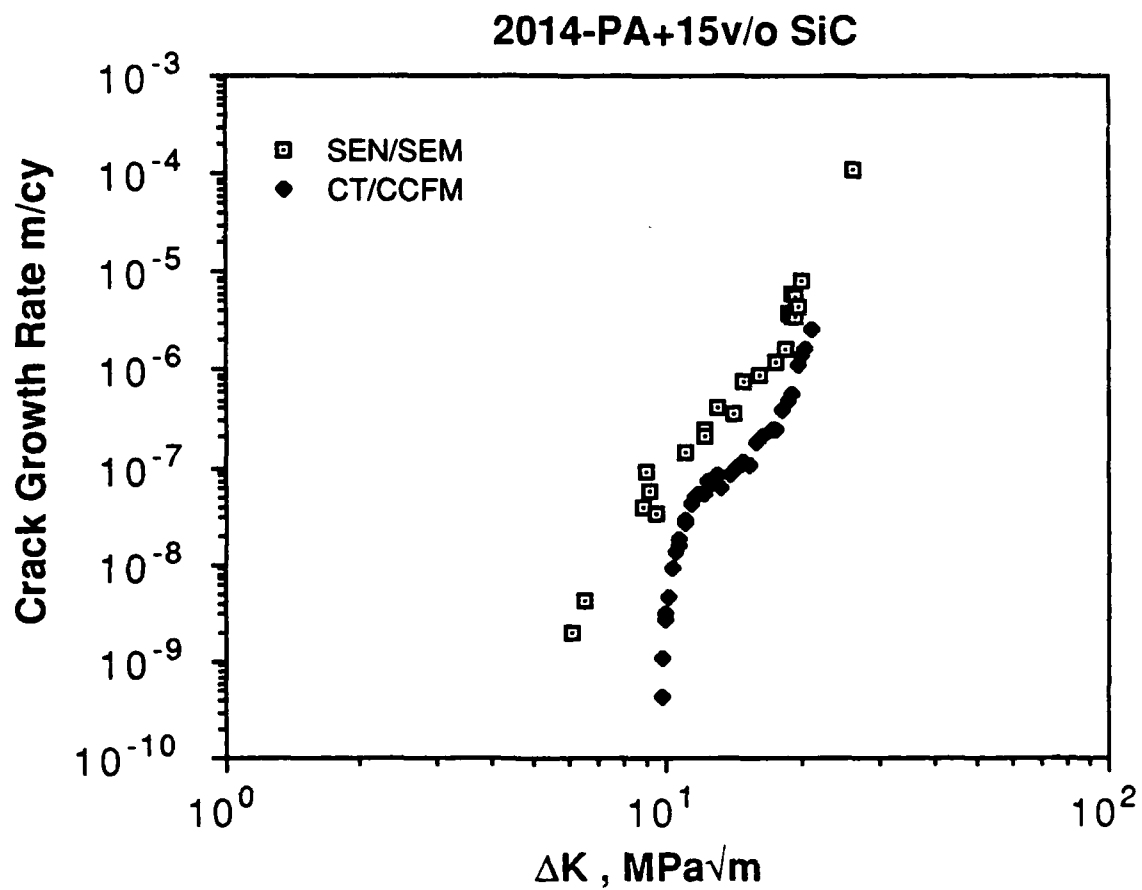


Fig. 5 Fatigue crack growth behavior of the composite. Both single edge notched (SEN) and compact tension (CT) specimens were tested. Differences are thought to be due to material variations.



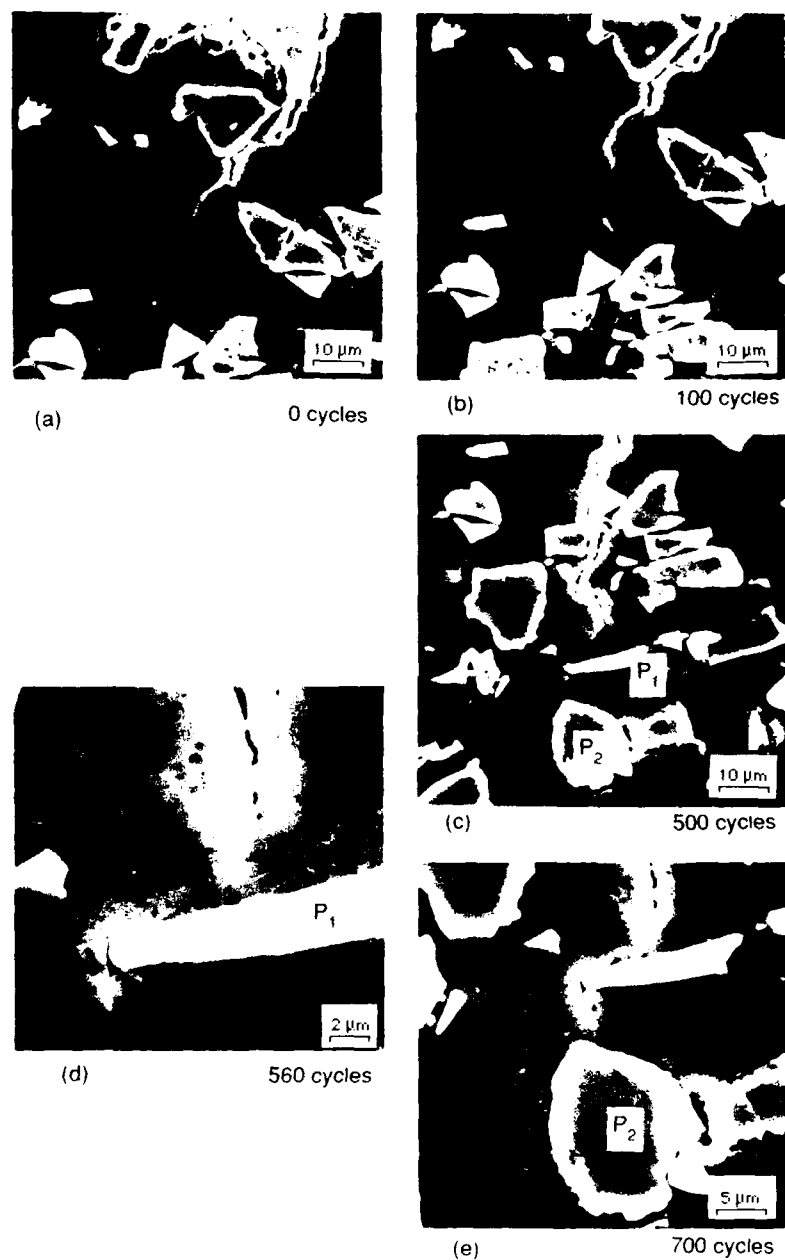


Fig. 6 Crack growth sequence for a fatigue crack interacting with SiC particles. Micromechanical interaction of the crack with particles  $P_1$  and  $P_2$  is shown in subsequent figures.

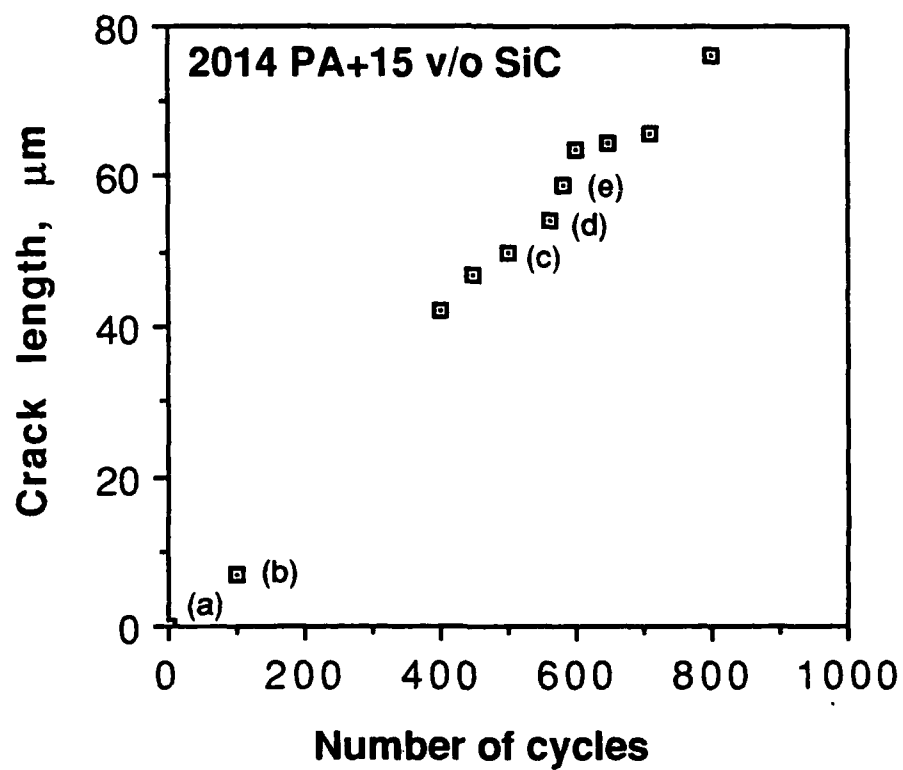


Fig. 7(a) Crack length as a function of loading cycles for the crack path shown in Fig. 6.

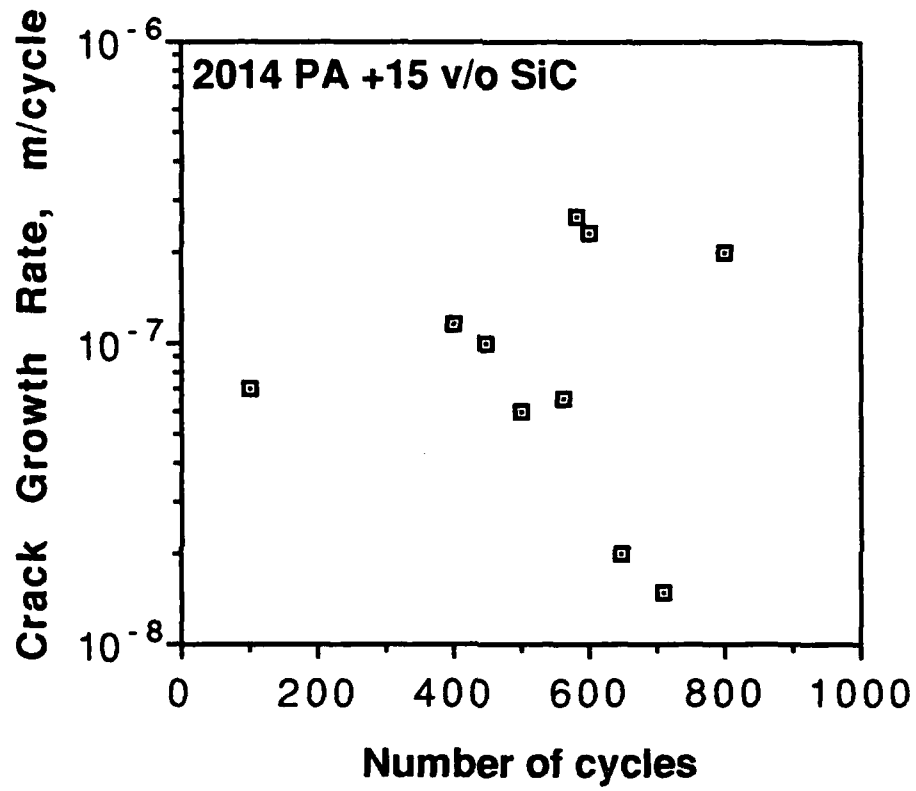
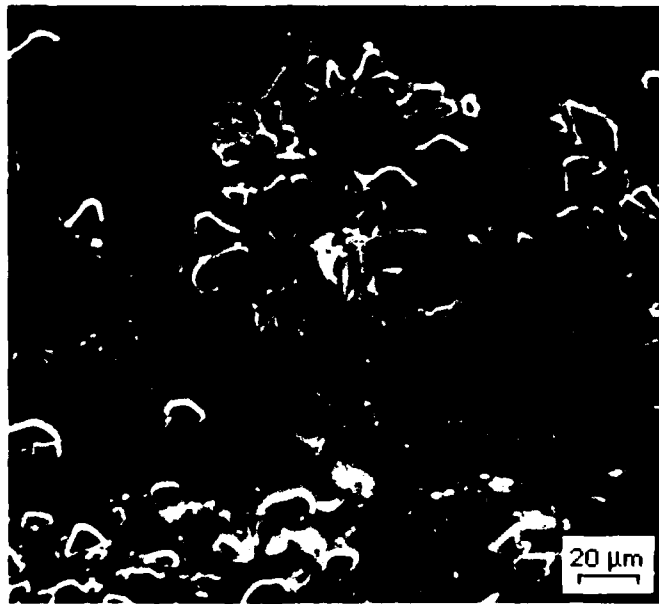
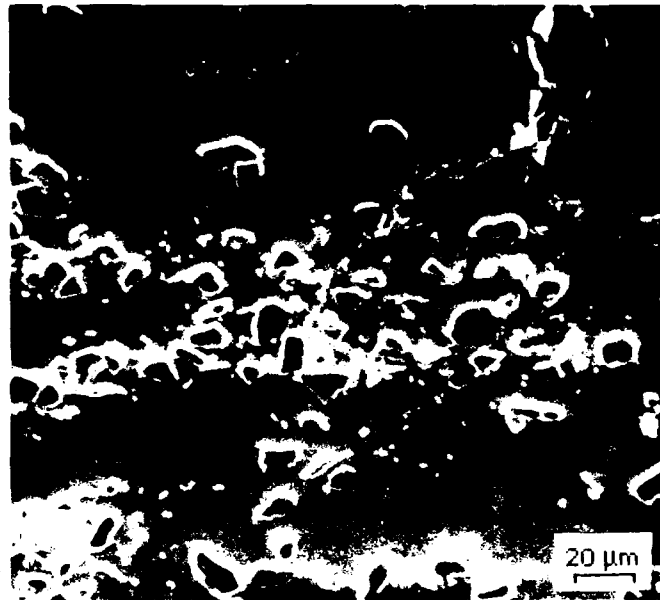


Fig. 7(b) Fatigue crack growth rates derived from the data in Fig. 7(a).



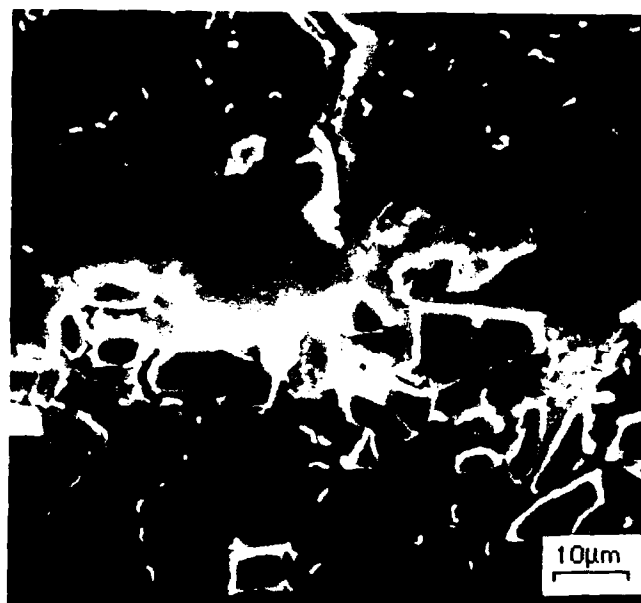
(a)



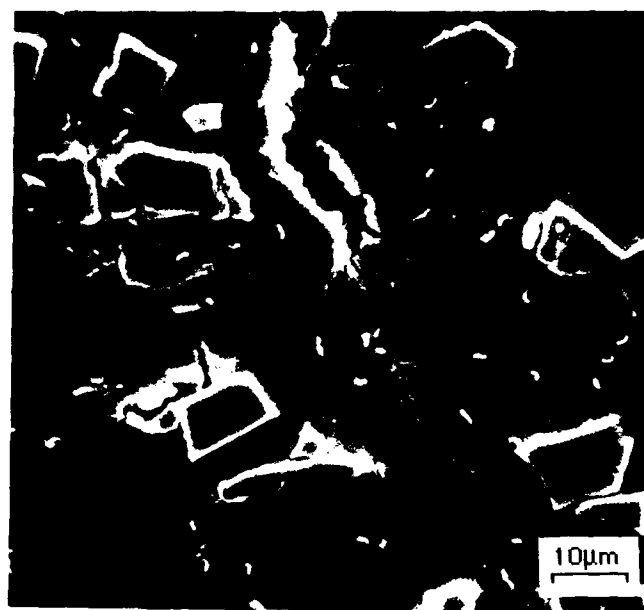
(b)

Fig. 8 Fatigue crack growth path at intermediate  $\Delta K = 16.2 \text{ MPa}\sqrt{\text{m}}$ .

(a) Crack tip relatively remote from SiC particles showing multiple crack tips, and (b) crack tip within a cluster of SiC particles showing a singular tip.



(a)



(b)

Fig. 9 Crack tips at about  $\Delta K = 19 \text{ MPa}\sqrt{\text{m}}$  showing multiple non-connected microcracks. Micromechanics analysis of (a) is shown in Fig. 17 and of (b) in Figs. 18 and 19.

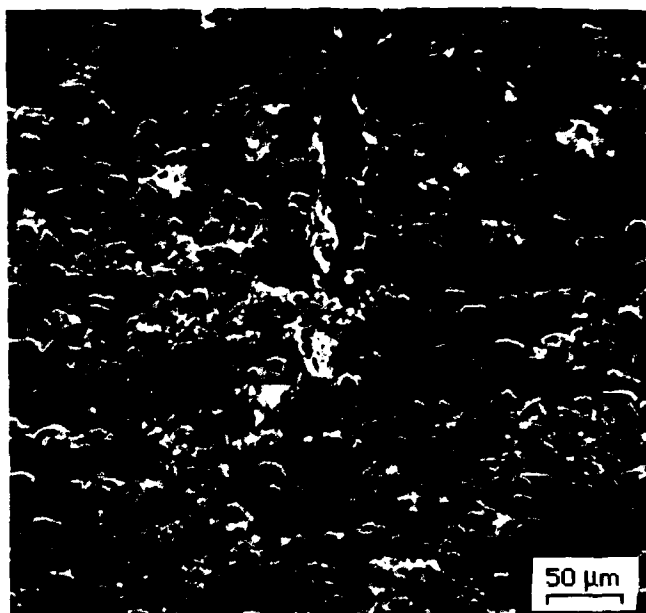


Fig. 10 Crack tip on the cycle preceding fast fracture. Location of crack tip is shown by the arrow.

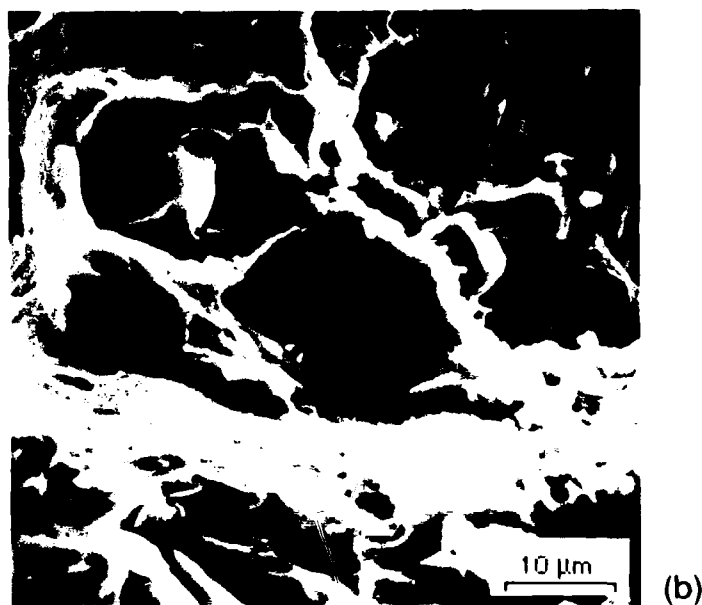
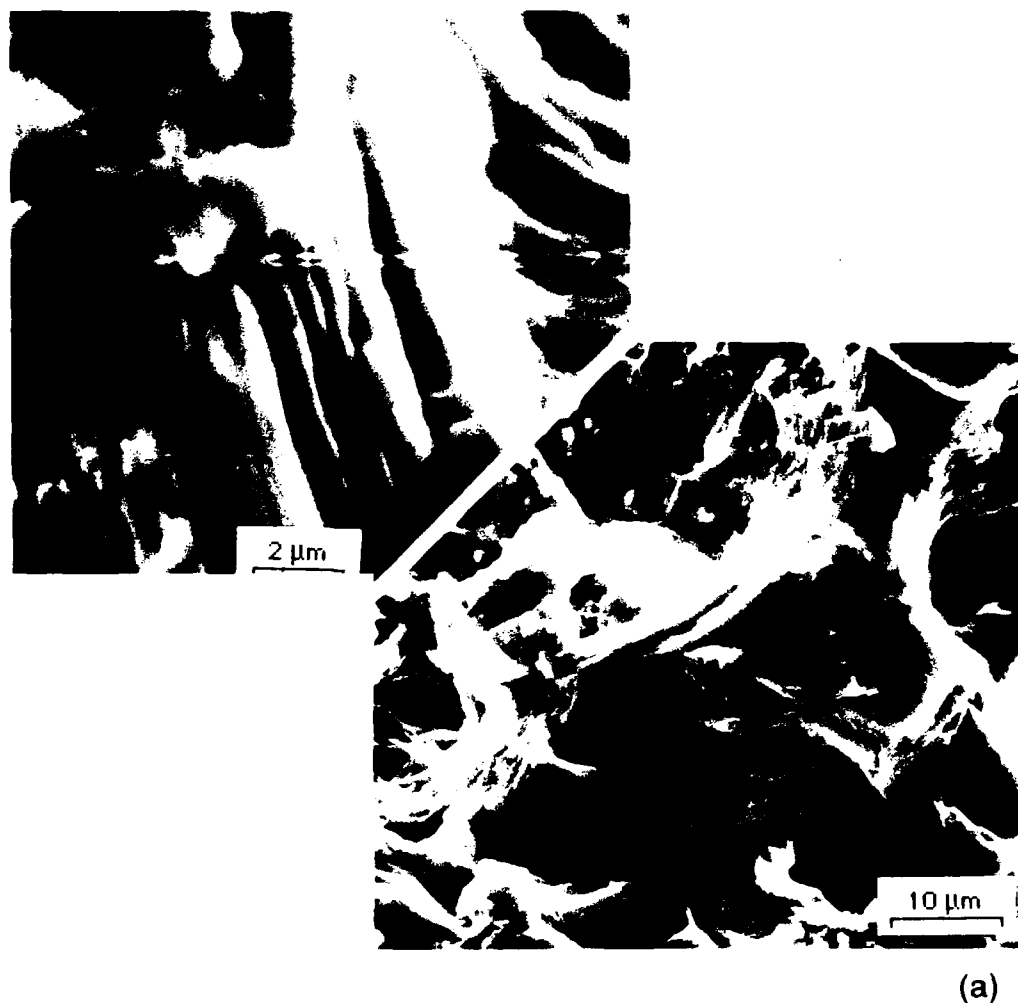


Fig. 11 Fractography of fatigue and fast fracture. (a) Fatigue region at  $\Delta K = 10 \text{ MPa}\sqrt{\text{m}}$  showing some of the few periodic crack arrest marks found. (b) Fast fracture region showing an example of a somewhat ductile rupture looking region.

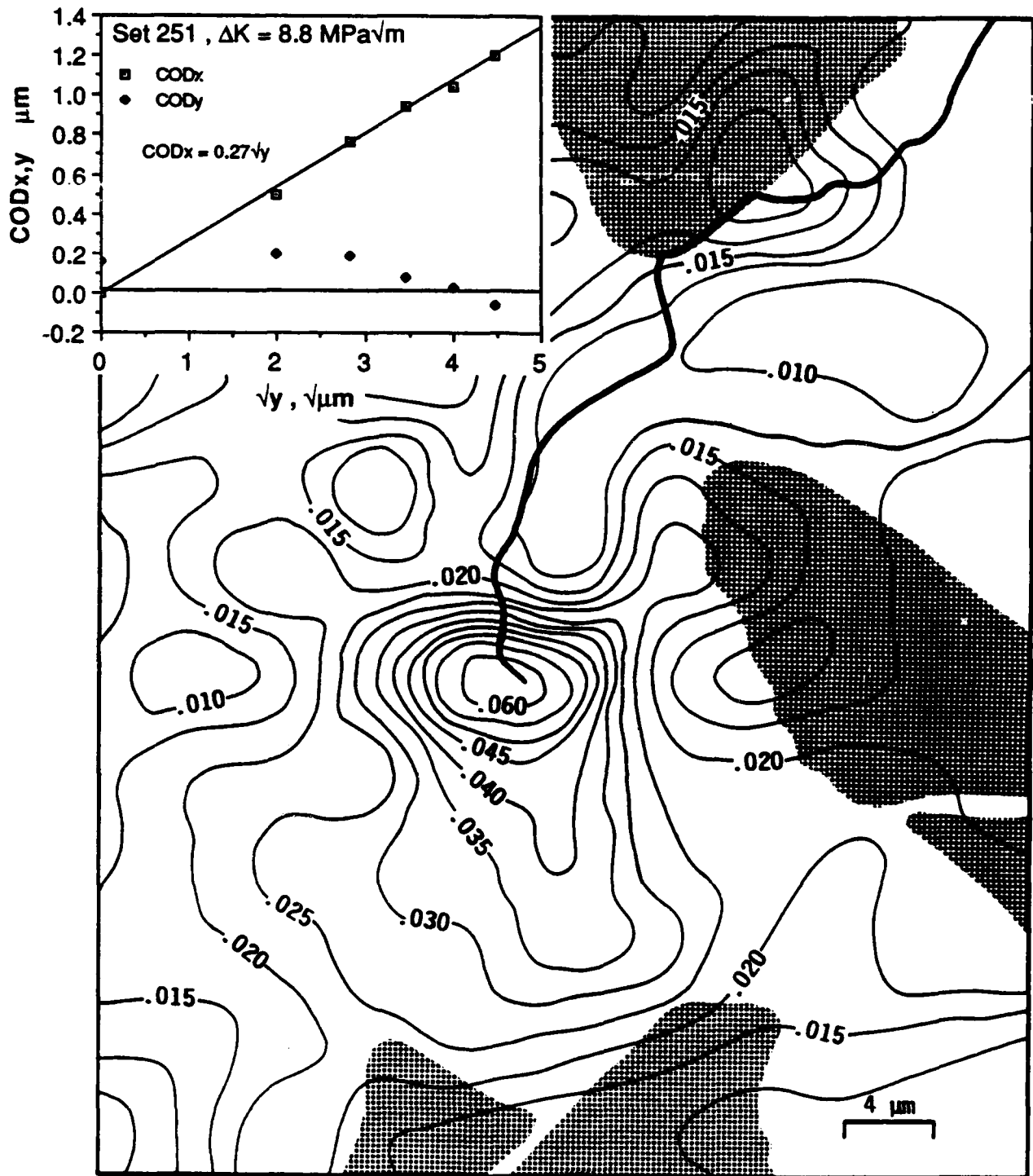


Fig. 12 Contour lines of maximum shear strain around the fatigue crack tip shown in Fig. 6(b), grown at  $\Delta K = 8.8 \text{ MPa}\sqrt{\text{m}}$ , which is relatively remote to SiC particles (shown as hatched regions). Strain distribution is similar to that for unreinforced material. The inset shows the crack opening displacements parallel (x) and perpendicular (y) to the loading direction.



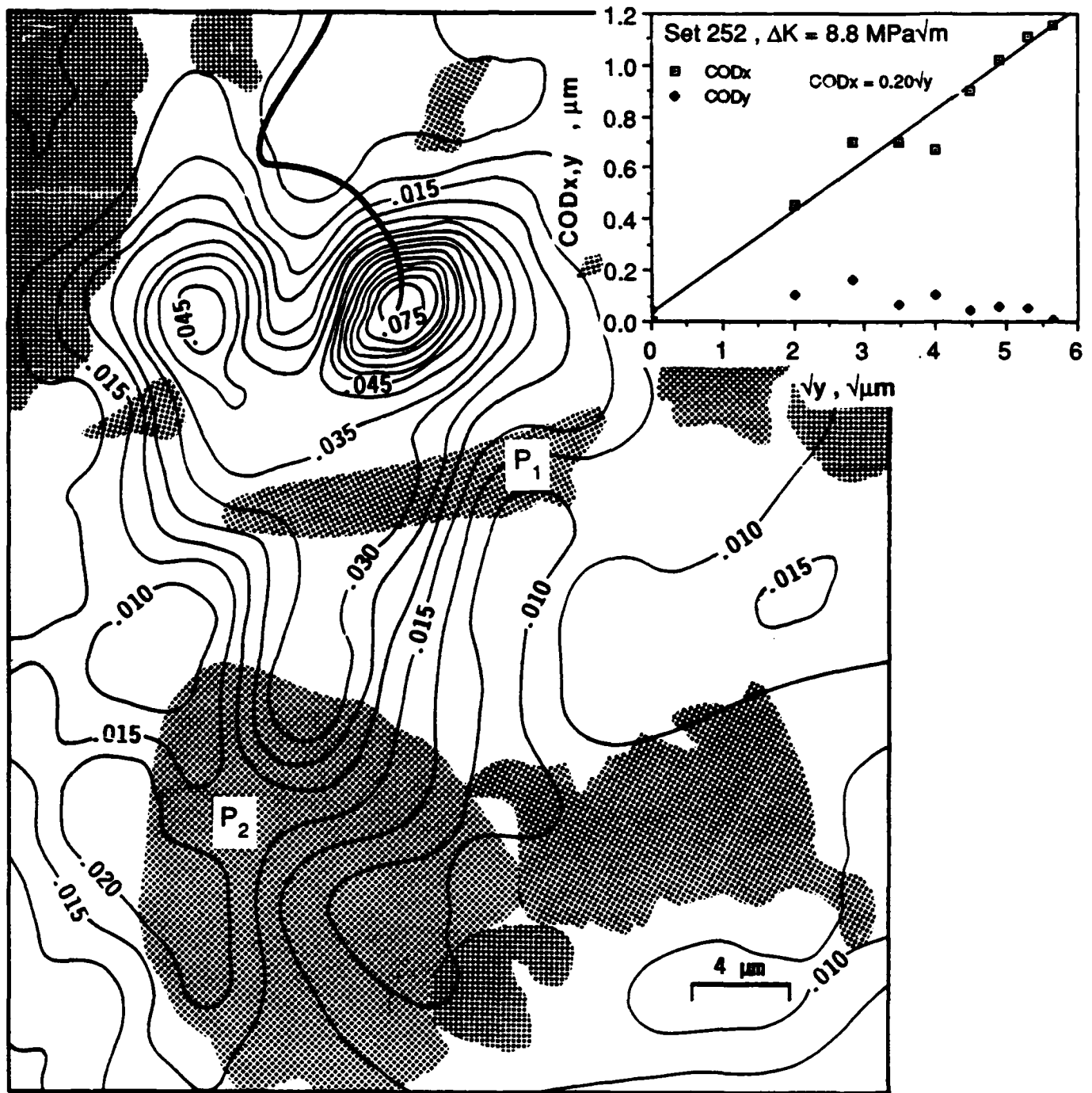


Fig. 13(a) Contour lines of maximum shear strain around the fatigue crack shown in Fig. 6(c), grown at  $\Delta K = 8.8 \text{ MPa}\sqrt{m}$ . Strains, measured at low spatial resolution, are similar to those for a crack in unreinforced material. The inset shows crack opening displacements.

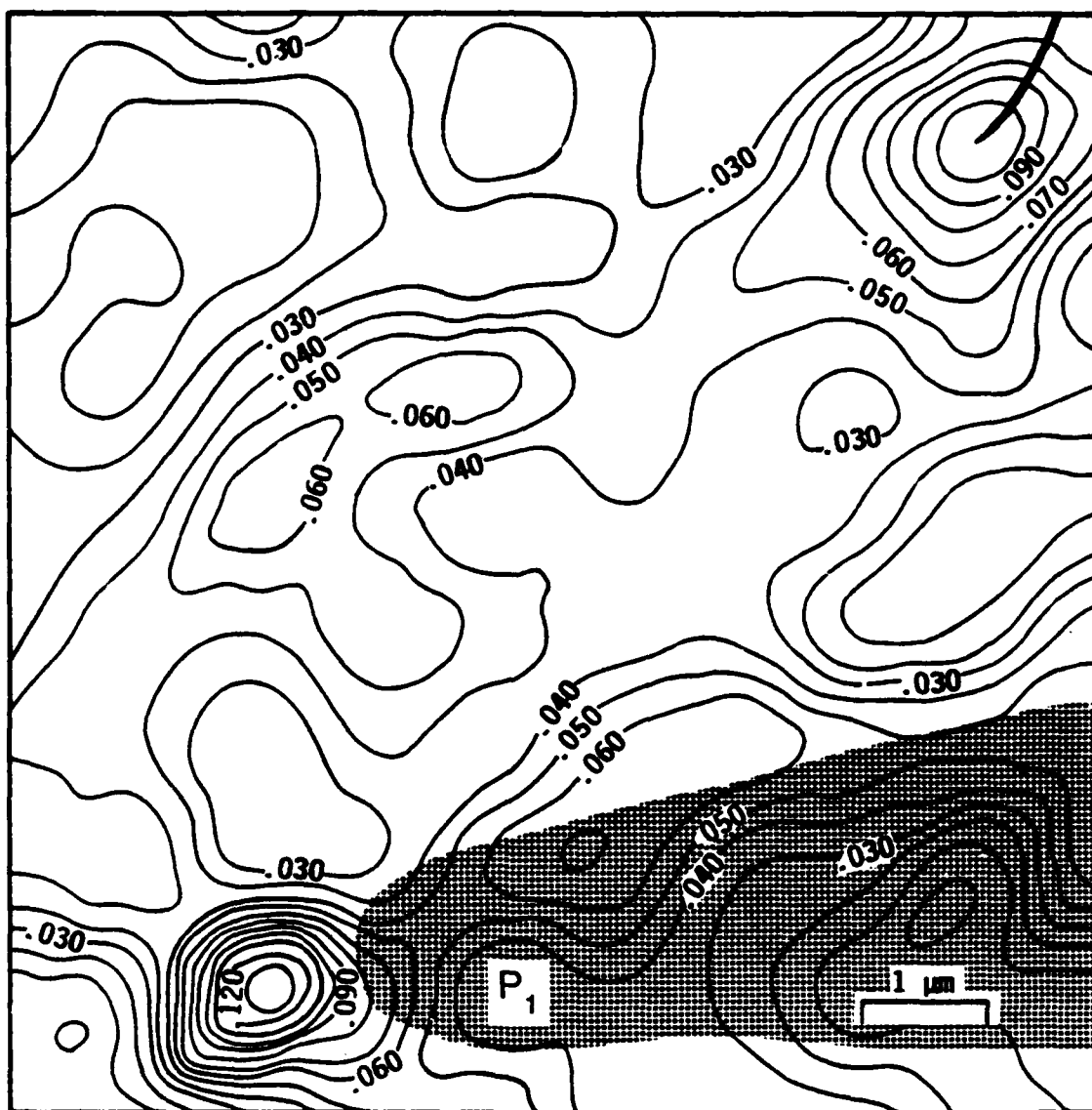


Fig. 13(b) A detail of the strains for the field in Fig. 13(a), measured with high resolution ( $0.25\ \mu\text{m}$ ), showing the concentration of maximum shear strain near the tip of the oblong SiC particle. Note the level of strain within the SiC particle.

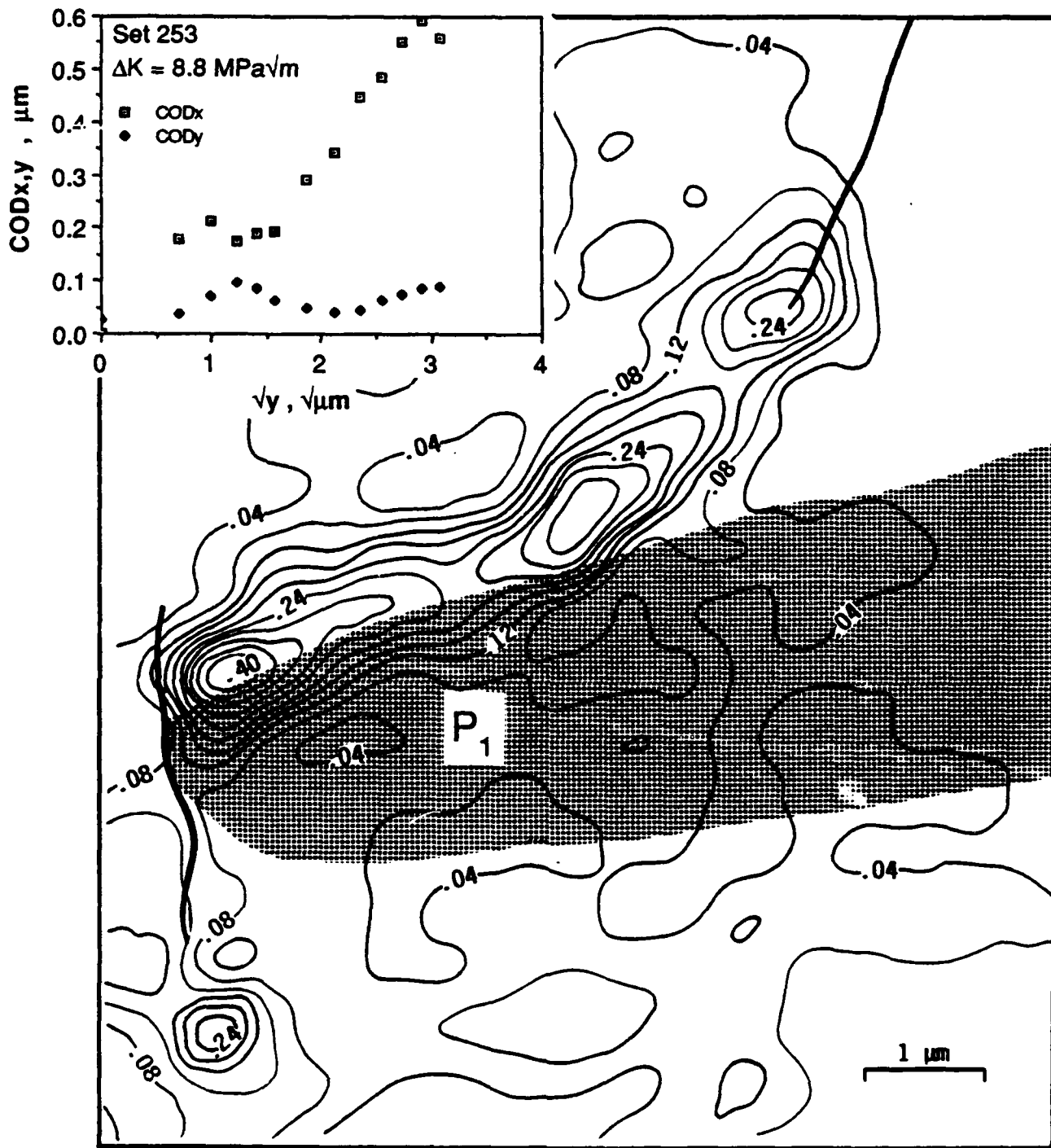


Fig. 14 Distribution of maximum shear strain for the fatigue crack shown in Fig. 6(d), grown at  $\Delta K = 8.8 \text{ MPa}\sqrt{m}$ . Strain is concentrating between the crack tip and the end of the SiC particle, where a microcrack has formed. Crack opening displacements are shown in the inset.

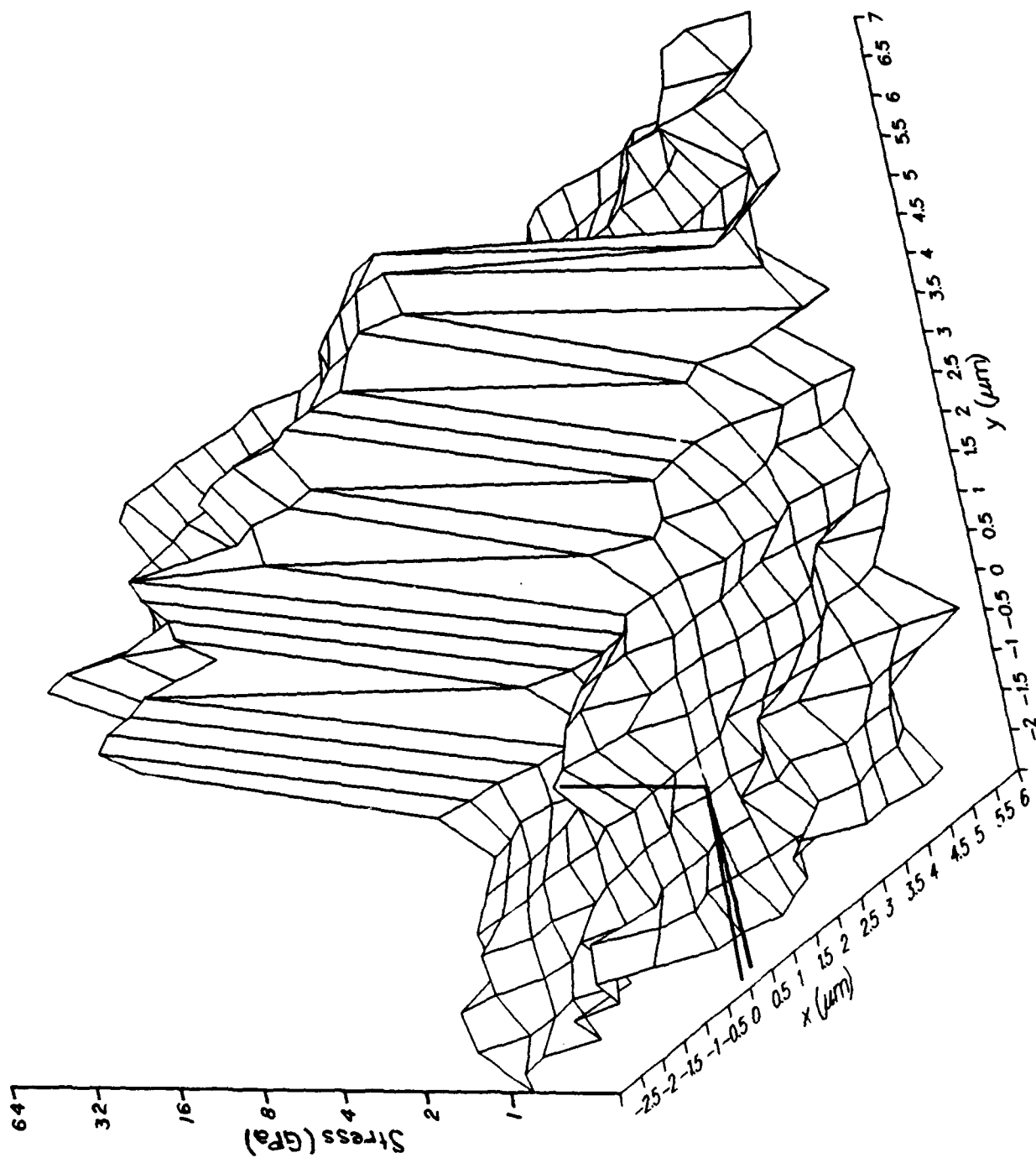


Fig. 15 Stresses computed from the strains shown in Fig. 14 showing the strong stress gradient across the matrix-particle interface. The field of view has been rotated relative to that in the previous figure in order to view the interface region. Crack tip is shown schematically. Note that the stress scale is logarithmic.

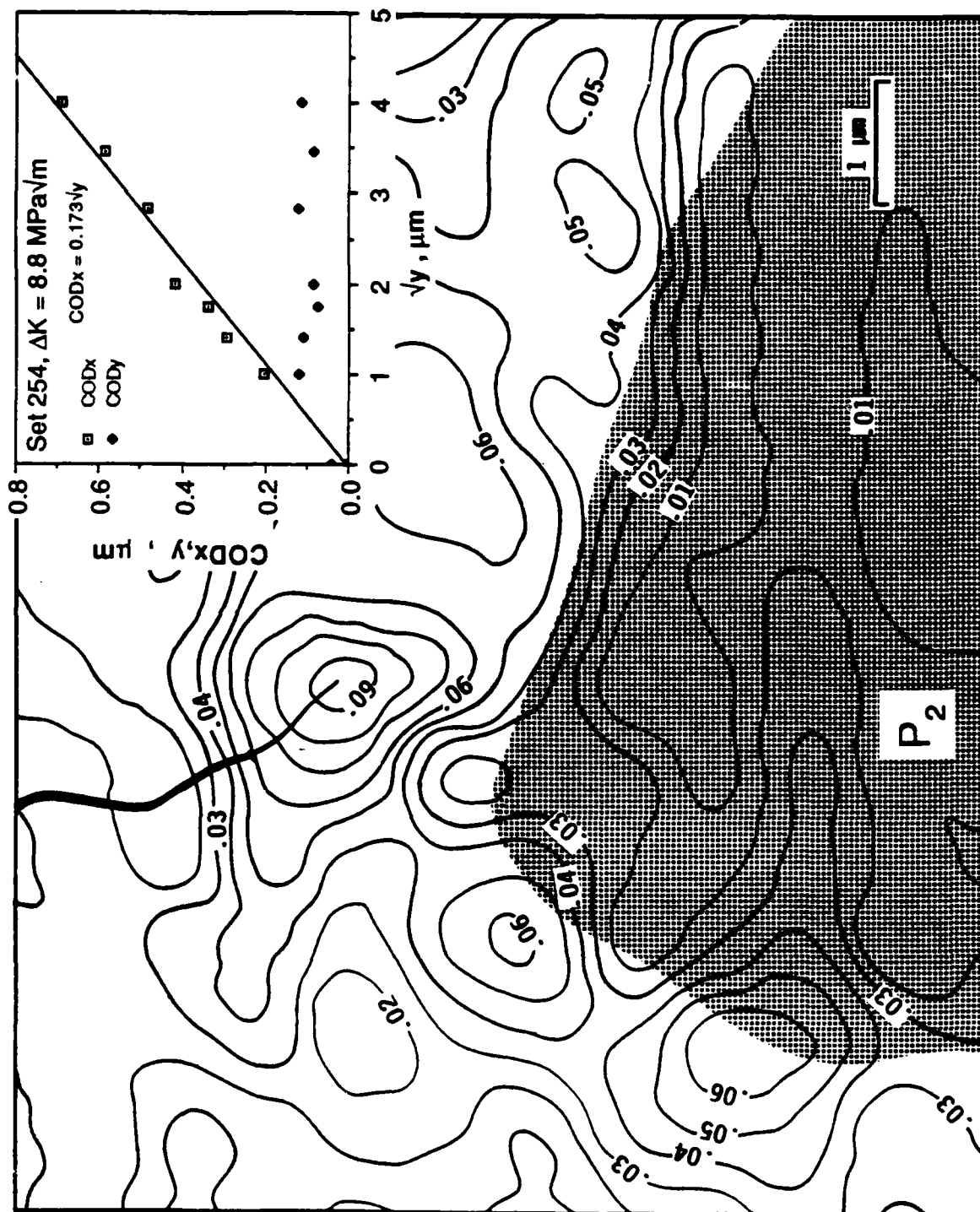


Fig. 16 Contours of maximum shear strain for a fatigue crack grown at  $\Delta K = 8.8 \text{ MPa}\sqrt{\text{m}}$  approaching particle  $P_2$ , as shown in Fig. 6(e). Inset shows the crack opening displacements. Proximity of the particle to the crack tip has again distorted the strain distribution.

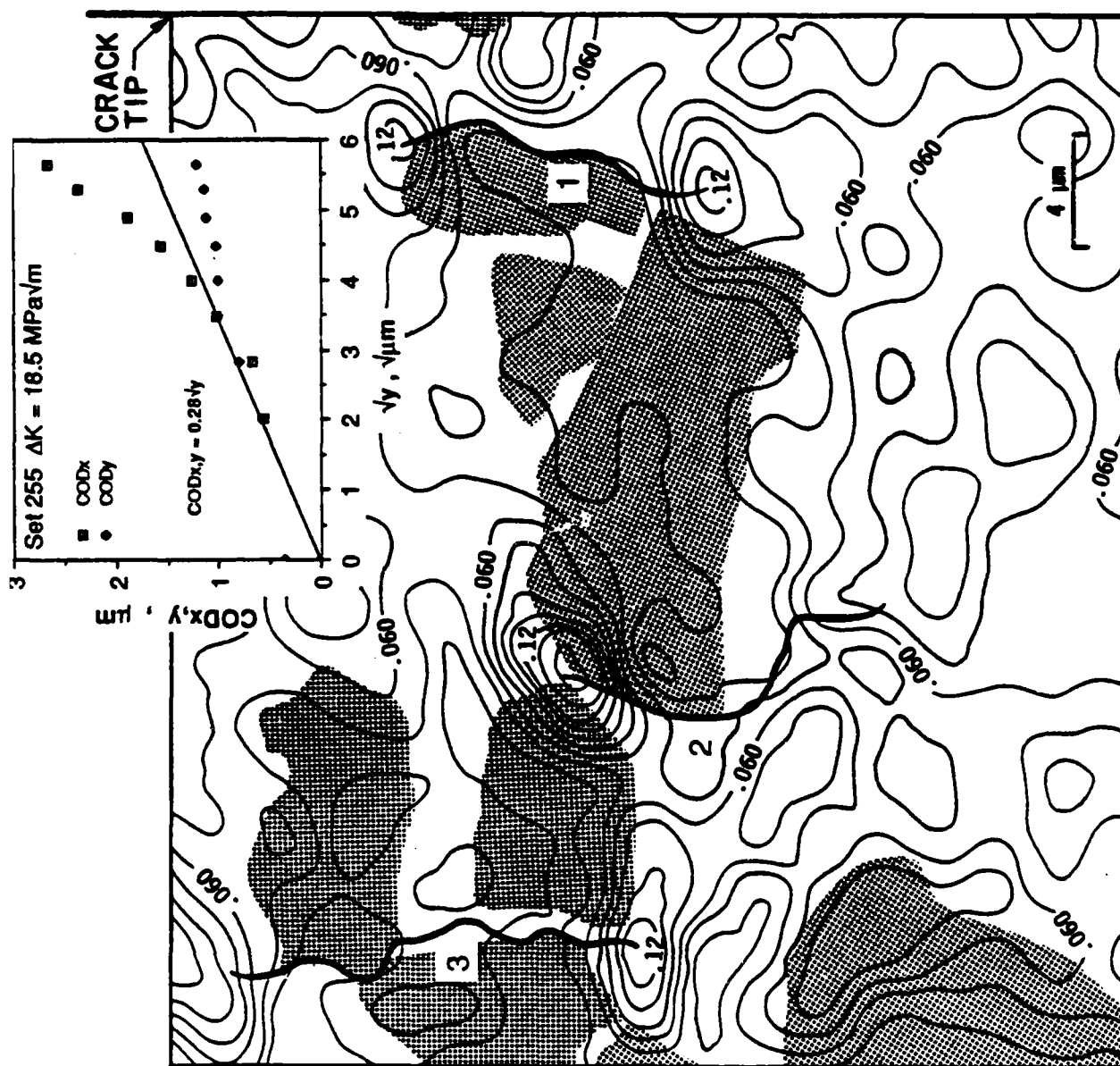


Fig. 17 Strain distribution for the fatigue crack, shown in Fig. 9, grown at  $\Delta K = 18.5 \text{ MPa}\sqrt{\text{m}}$  and having several non-connected microcracks. Note the strain concentrations at the tips of the microcracks and the mixed mode nature of the crack opening displacements (inset).

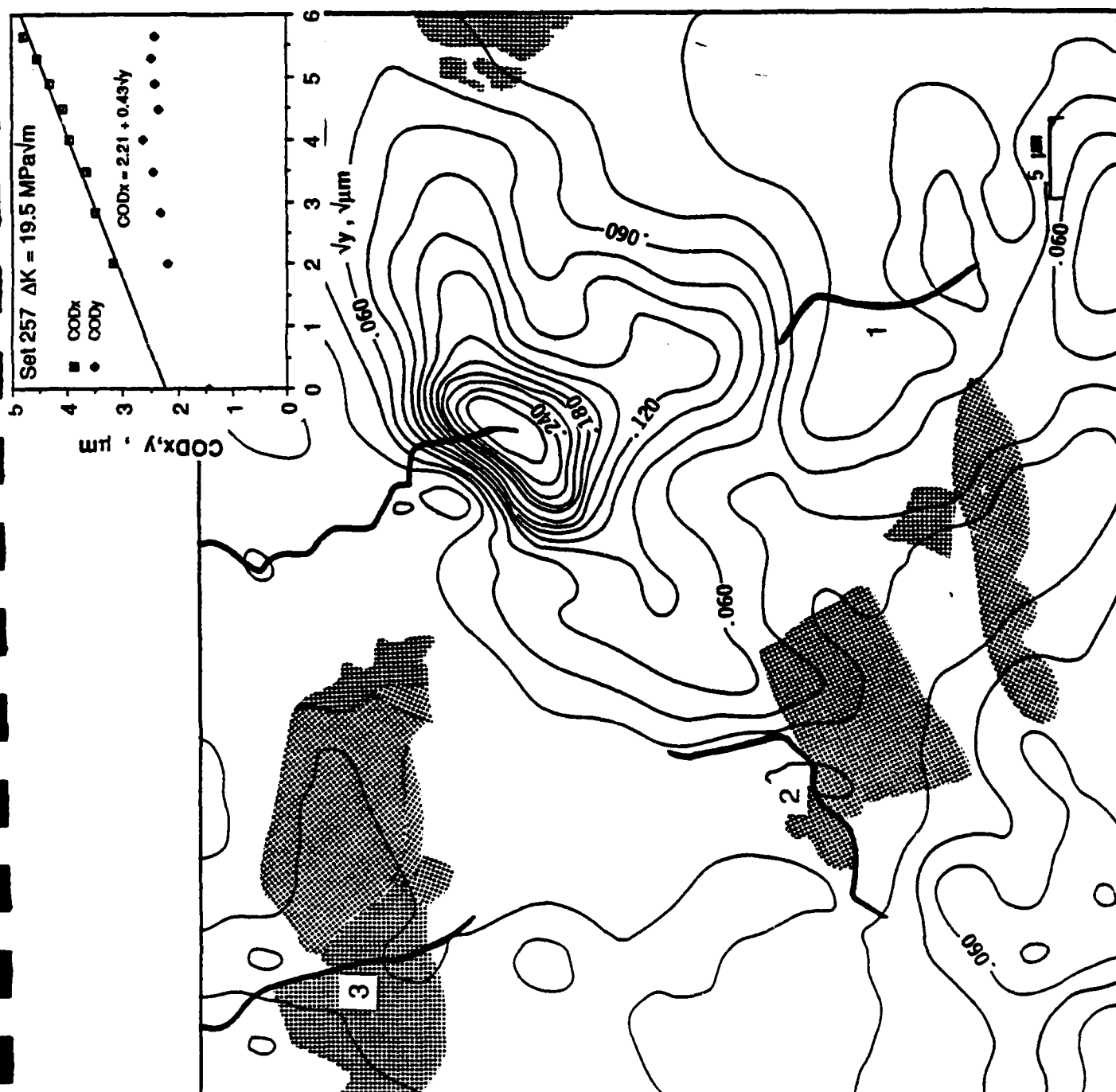


Fig. 18 Strain distribution for a fatigue crack grown at  $\Delta K = 19.5 \text{ MPa}\sqrt{\text{m}}$  having several non-connected microcracks. Strain in this field is concentrated at the tip of the main crack. Note the blunt characteristic of the crack tip (inset).

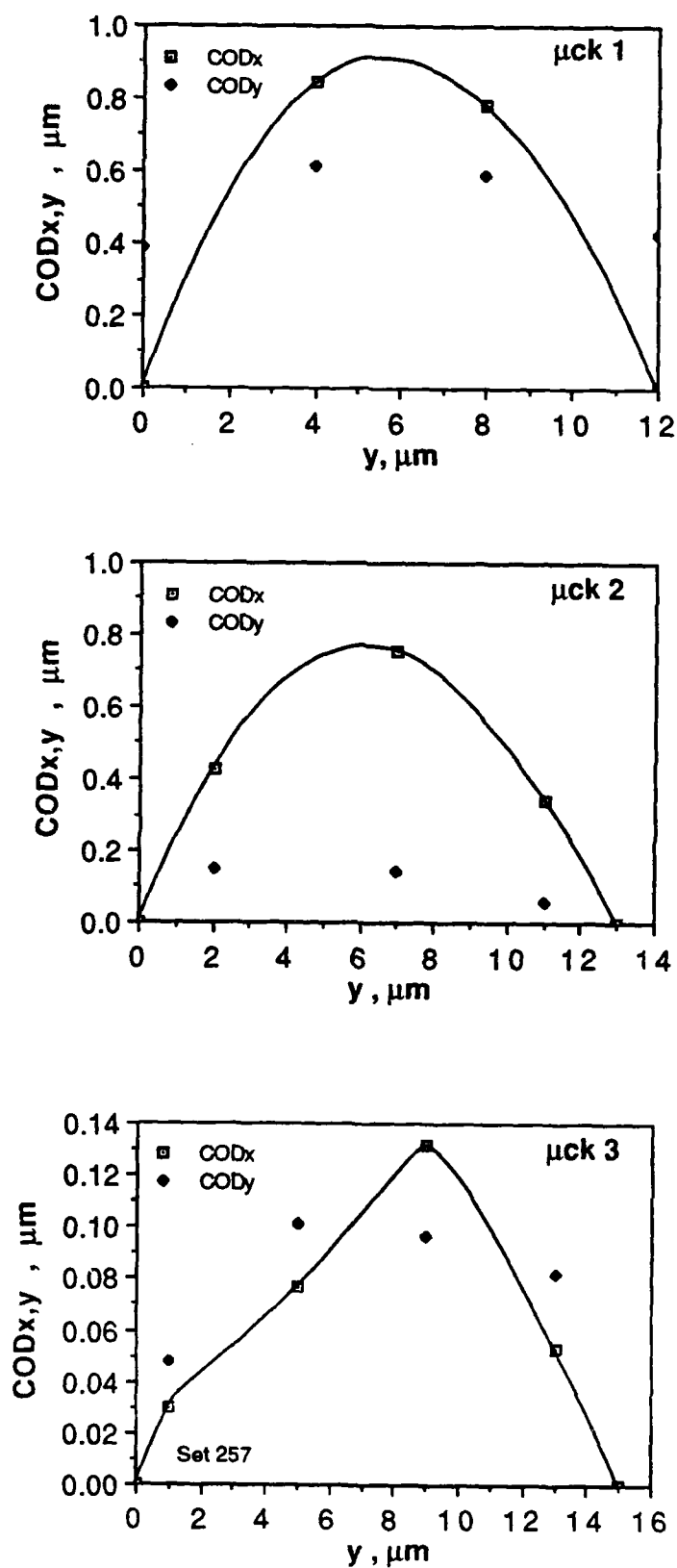


Fig. 19 Crack opening displacements for the microcracks of Fig. 18. Note the large components of Mode II in cracks 1 and 3.



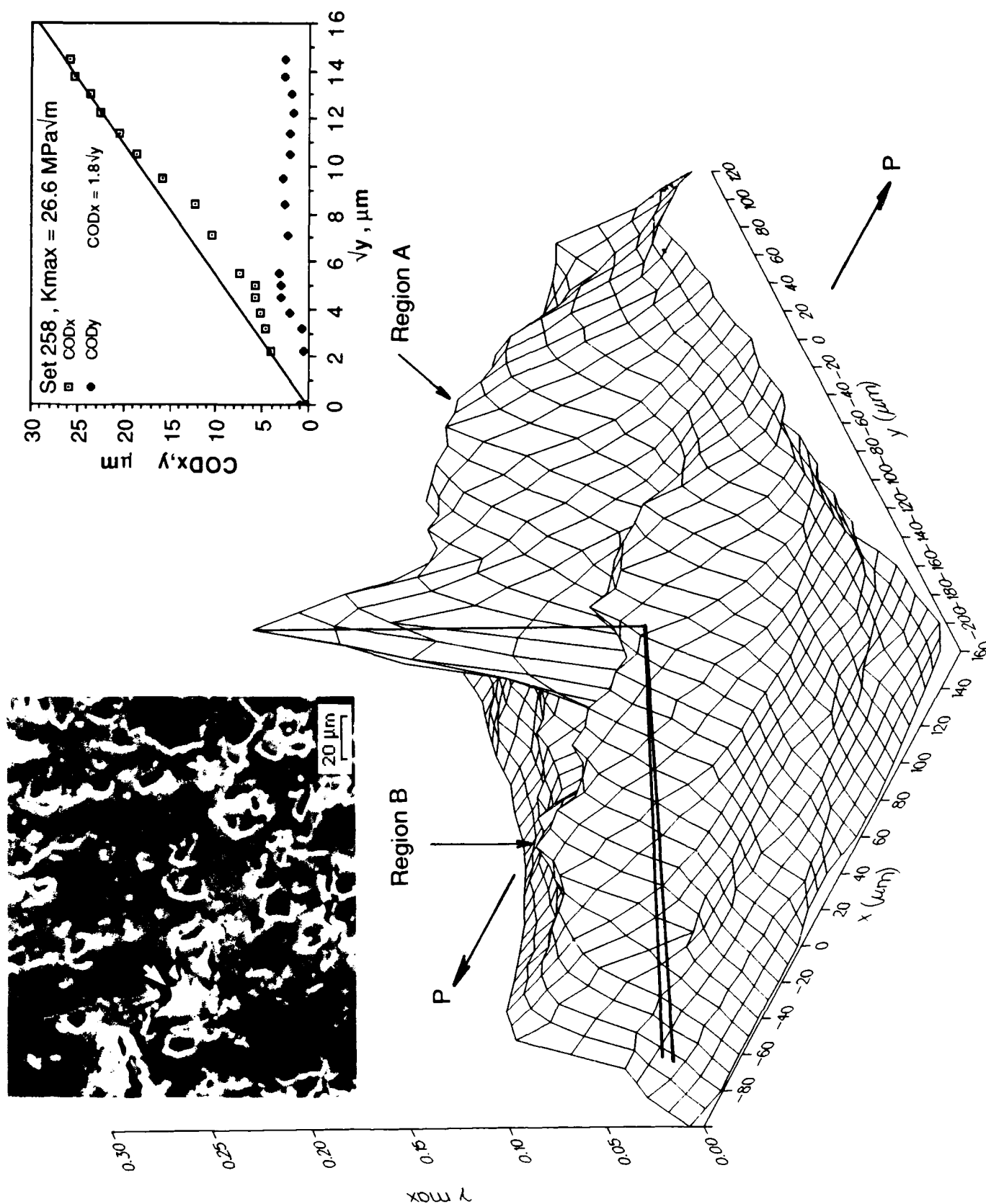


Fig. 20 Distribution of maximum shear strain around the crack tip, shown in the inset, just prior to final fracture. Crack is shown on the plane of zero strain. Region A shows large strains ahead of the crack tip, but there are also relatively large strains along the crack wake (Region B). Crack opening displacements are shown in the inset.

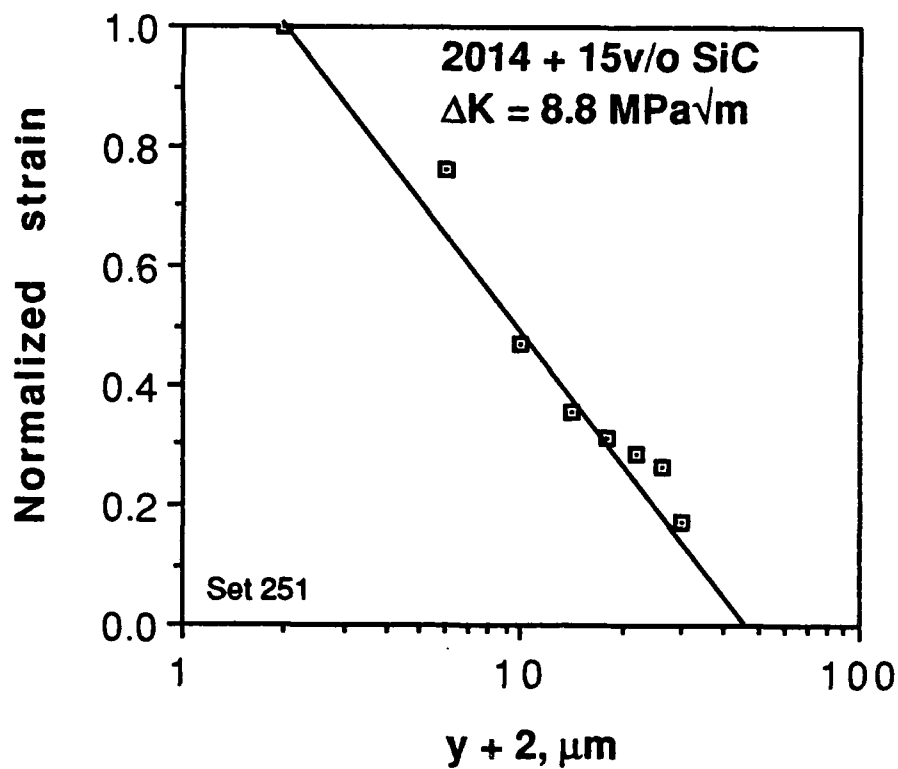


Fig. 21(a) Distribution of effective strain (normalized by the crack tip strain) ahead of the fatigue crack shown in Figs. 6(b) and 12. The line represents the fit of eq. (3) to the data.

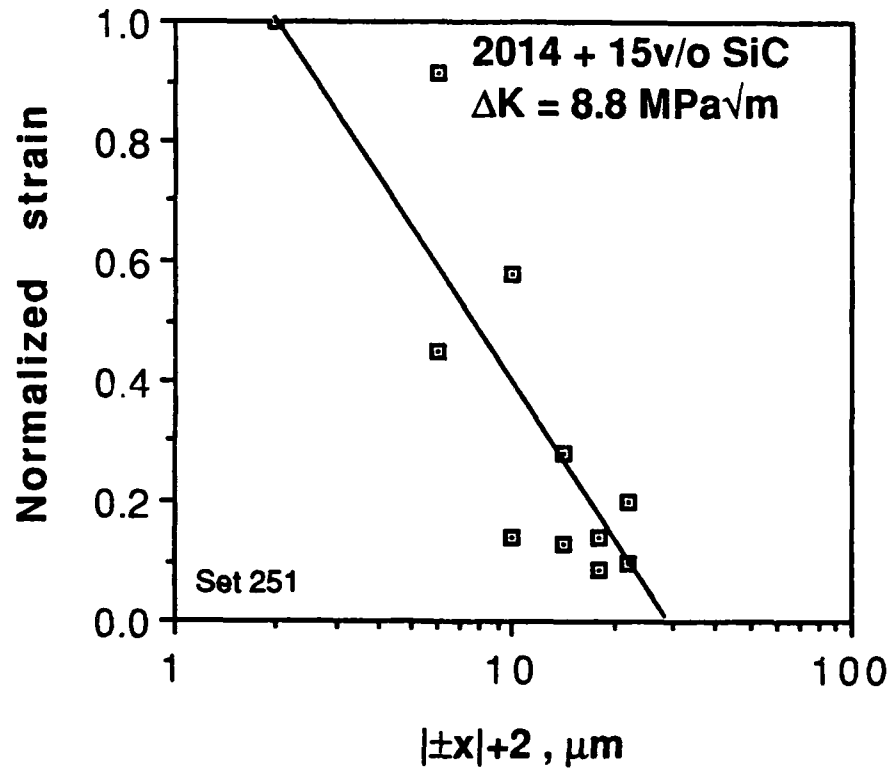


Fig. 21(b) Distribution of effective strain (normalized by the crack tip strain) perpendicular to the loading axis for the fatigue crack shown in Figs. 6(b) and 12. The line represents the fit of eq. (3) to the data.

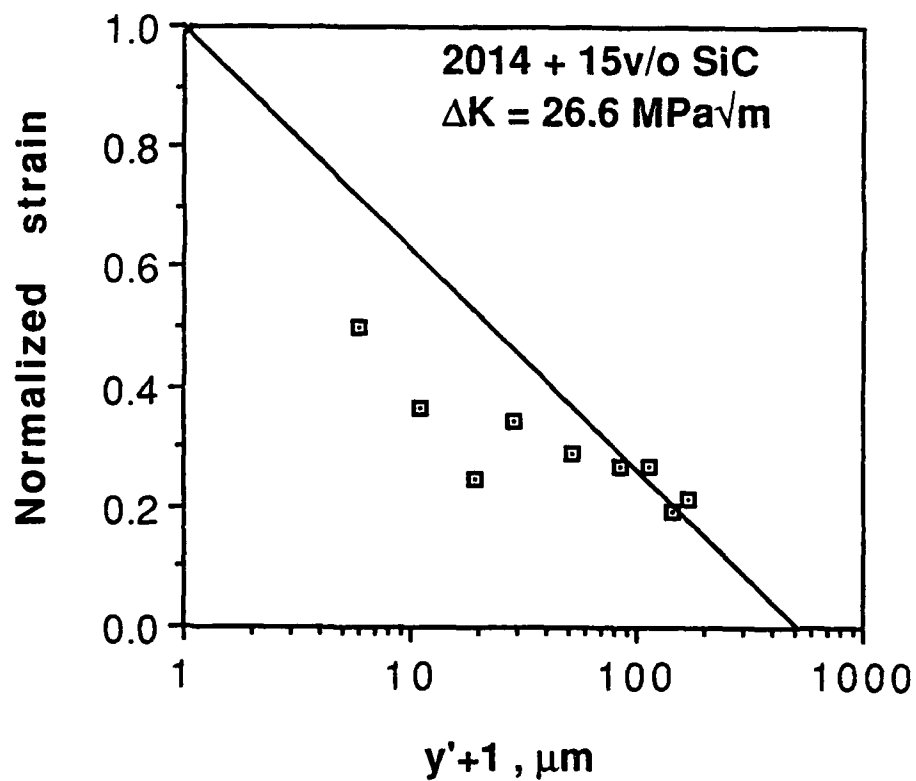


Fig. 22(a) Distribution of effective strain (normalized by the crack tip strain) ahead of the crack shown in Figs. 10 and 20. The line represents the fit of eq. (3) to the data farthest from the crack tip.

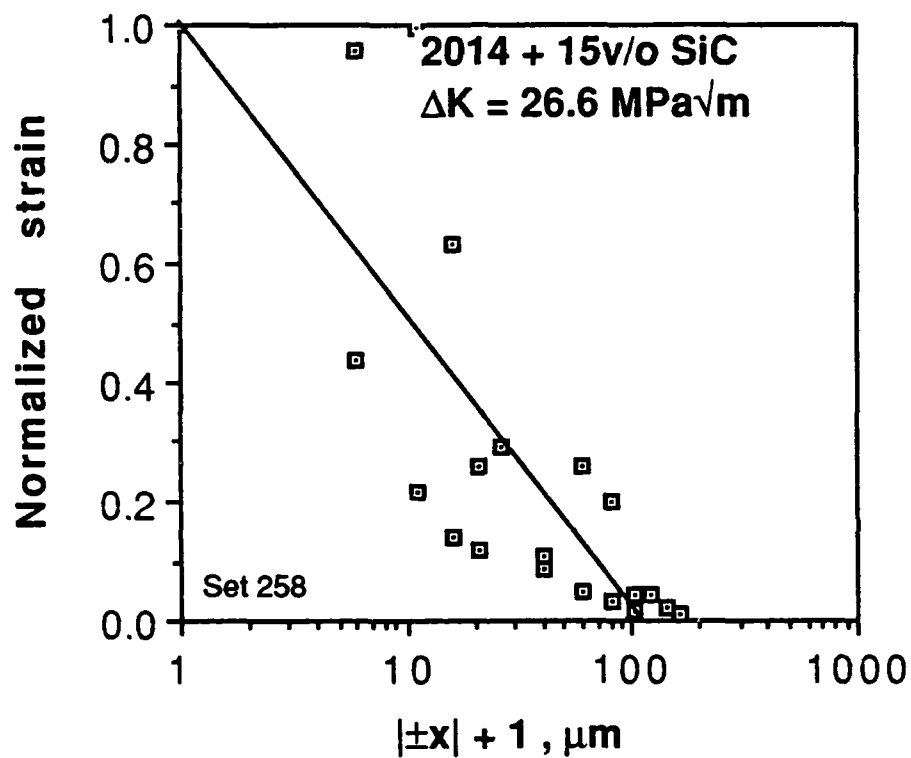


Fig. 22(b) Distribution of effective strain (normalized by the crack tip strain) perpendicular to the loading axis for the fatigue crack shown in Figs. 10 and 20. The line represents the fit of eq. (3) to the data.

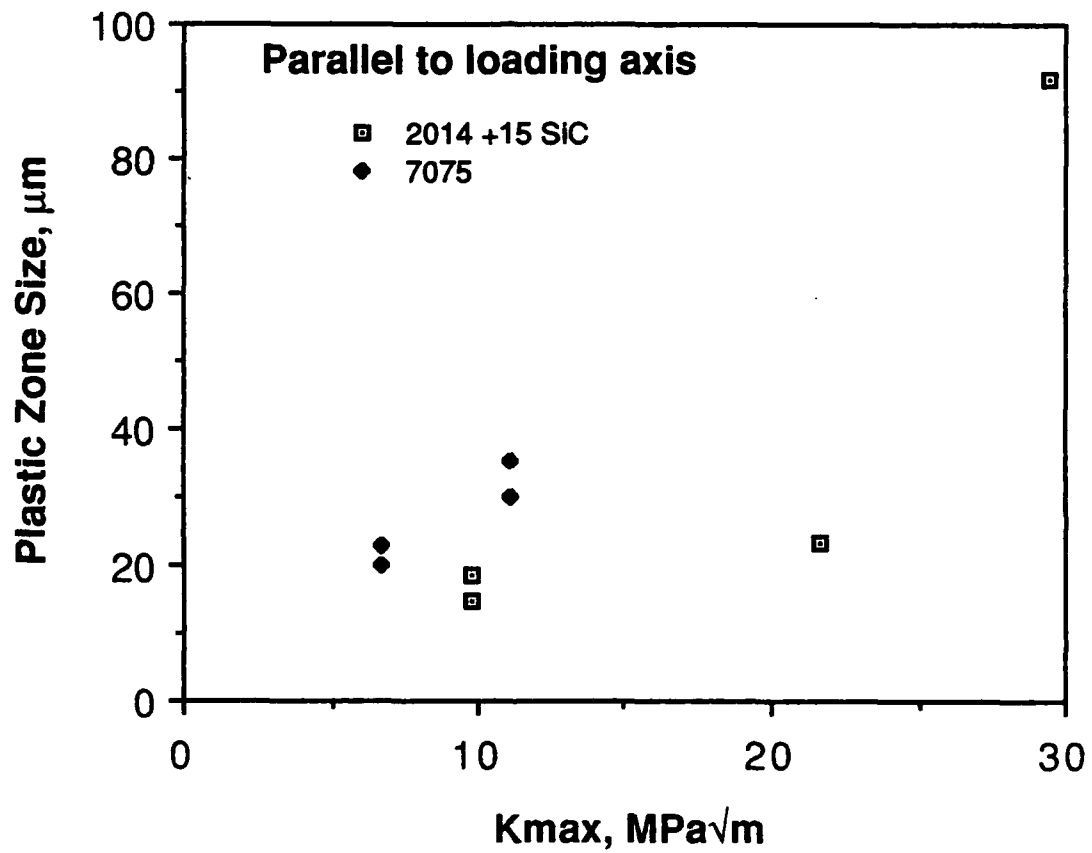


Fig. 23 Plastic zone sizes parallel to the loading axis for the composite compared to those for fatigue cracks in unreinforced 7075-T651.

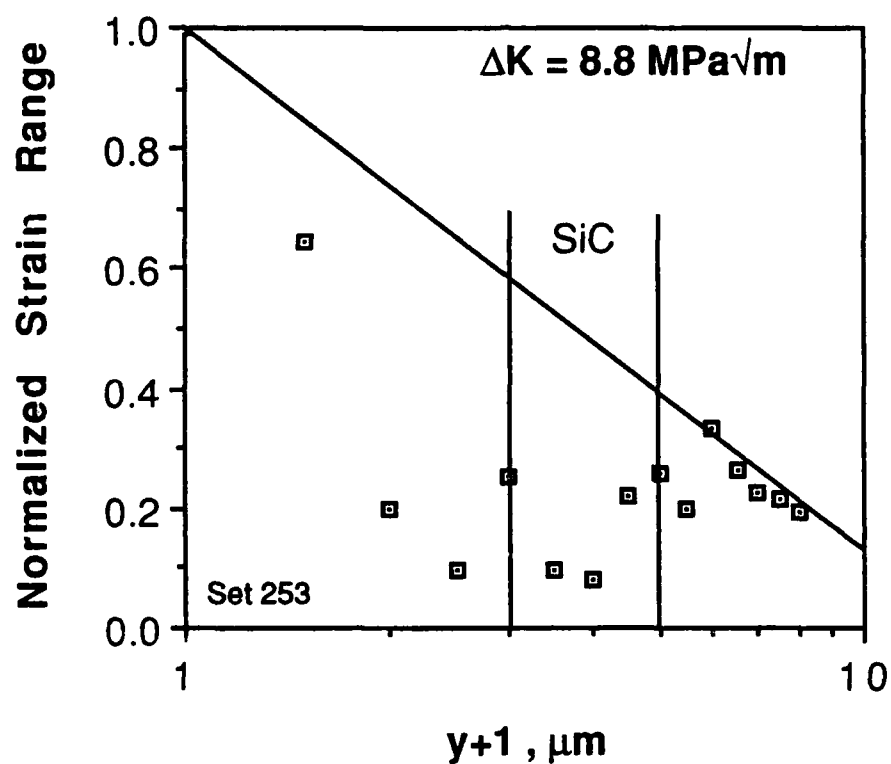


Fig. 24 Alteration of the distribution of effective strain (normalized by the crack tip strain) ahead of the crack shown in Figs. 6(d) and 14 (a) by the SiC particle. The line represents the fit of eq. (3) to the data farthest from the crack tip.

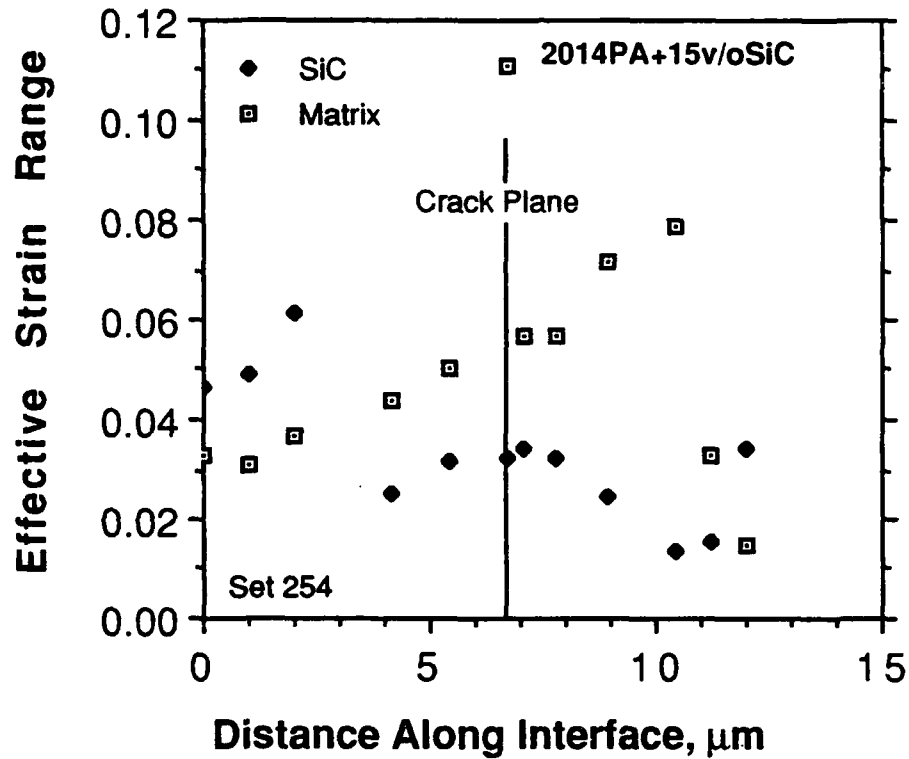


Fig. 25 Distribution of effective strain along each side of SiC particle  $P_2$ , shown in Figs. 6(e) and 16, going from left to right across the plane of the crack. Strain magnitude ratio along the loading axis is reversed to that ahead of the crack tip.



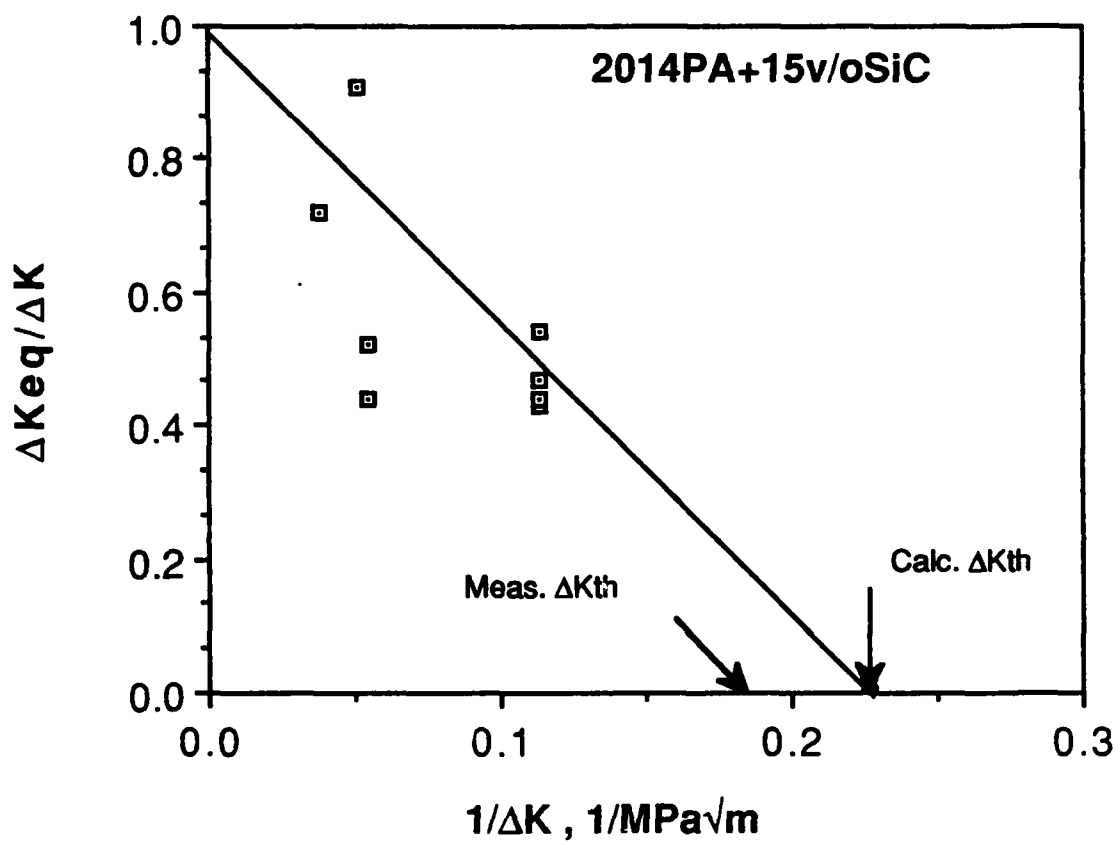


Fig. 26 Determination of crack closure from measured crack tip parameters and computed  $\Delta K_{th}$ .

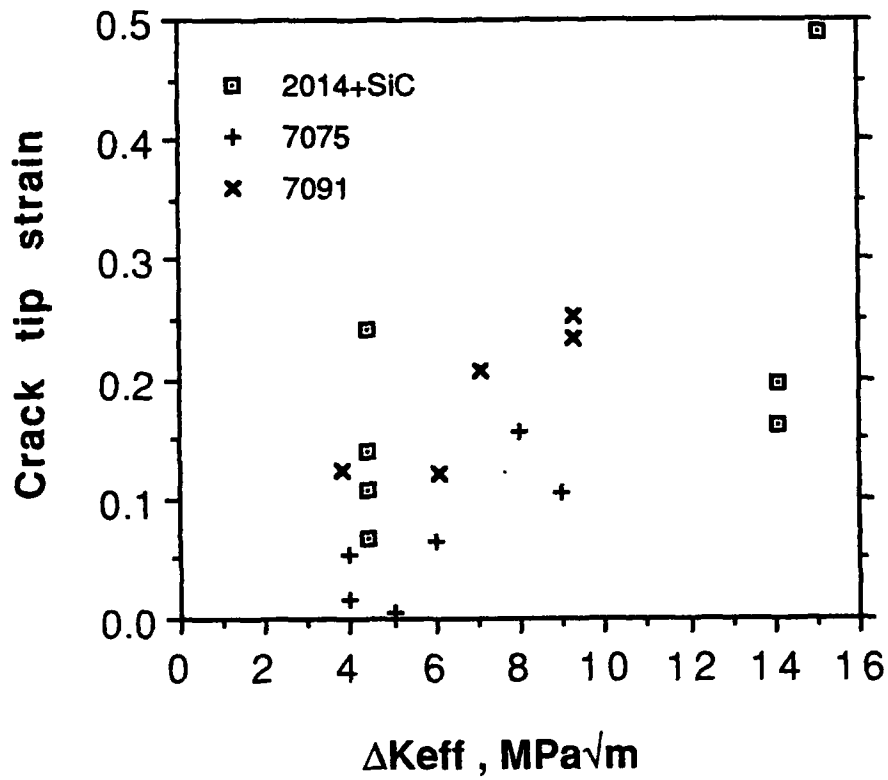


Fig. 27 Comparison of crack tip strains for the composite to those for unreinforced aluminum alloys showing the similarities in magnitude.